



biblio.ugent.be

The UGent Institutional Repository is the electronic archiving and dissemination platform for all UGent research publications. Ghent University has implemented a mandate stipulating that all academic publications of UGent researchers should be deposited and archived in this repository. Except for items where current copyright restrictions apply, these papers are available in Open Access.

This item is the archived peer-reviewed author-version of: Continuous direct compression as manufacturing platform for sustained release tablets

Authors: Van Snick B., Holman J., Cunningham C., Kumar A., Vercruyse J., De Beer T., Remon J.P., Vervaet C.

In: International Journal of Pharmaceutics 2017, 519(1-2): 390-407

To refer to or to cite this work, please use the citation to the published version:

Van Snick B., Holman J., Cunningham C., Kumar A., Vercruyse J., De Beer T., Remon J.P., Vervaet C. (2017)

Continuous direct compression as manufacturing platform for sustained release tablets

In-vivo evaluation of apocynin for prevention of Helicobacter pylori-induced gastric.

International Journal of Pharmaceutics 519(1-2): 390-407

DOI: 10.1016/j.ijpharm.2017.01.010

Continuous direct compression as manufacturing platform for sustained release tablets

Authors

B. Van Snick¹, J. Holman², C. Cunningham³, A. Kumar⁴, J. Vercruysse¹, T. De Beer⁴, J.P. Remon¹, C. Vervaet¹

¹Laboratory of Pharmaceutical Technology, Ghent University, Ghent, Belgium.

²GEA APC Pharma Solids, Eastleigh, United Kingdom.

³Colorcon Inc., Harleysville, PA, USA

⁴Laboratory of Process Analytical Technology, Ghent University, Ghent, Belgium

Corresponding author:

Institution: Laboratory of Pharmaceutical Technology

Address: Ghent University, Ottergemsesteenweg 460, 9000, Gent, Belgium

Tel: 0032 9 264

Fax: 0032 9 264

e-mail: chris.vervaet@ugent.be

Abstract

This study presents a framework for process and product development on a continuous direct compression manufacturing platform. A challenging sustained release formulation with high content of a poorly flowing low density drug was selected. Two HPMC grades were evaluated as matrix former: standard Methocel CR and directly compressible Methocel DC2. The feeding behavior of each formulation component was investigated by deriving feed factor profiles. The maximum feed factor was used to estimate the drive command which strongly depended upon the density of the material. Furthermore, the shape of the feed factor profile allowed definition of a customized refill regime for each material. Inline NIRs was used to estimate the residence time distribution (RTD) in the mixer and monitor blend uniformity. Tablet content and weight variability were determined as additional measures of mixing performance. For CR, the best axial mixing (i.e. feeder fluctuation dampening) was achieved when an impeller with high number of radial mixing blades operated at low speed. However, the variability in tablet weight and content uniformity deteriorated under this condition. One can therefore conclude that balancing axial mixing with tablet quality is critical for Methocel CR. However, reformulating with the direct compressible Methocel DC2 as matrix former improved tablet quality vastly. Furthermore, both process and product were significantly more robust to changes in process and design variables. This observation underpins the importance of flowability during continuous blending and die-filling. At the compaction stage, blends with Methocel CR showed better tableability driven by a higher compressibility as the smaller CR particles have a higher bonding area. However, tablets of similar strength were achieved using Methocel DC2 by targeting equal porosity. Compaction pressure impacted tablet properties and dissolution. Hence controlling thickness during continuous manufacturing of sustained release tablets was crucial to ensure reproducible dissolution.

List of abbreviations

CI	compressibility index
$C_{in}(t)$	tracer concentration in the inlet stream
$C_{out}(t)$	tracer concentration in the outlet stream predicted by macro-mixing model
$c(t)$	concentration profile RTD
d	tablet diameter
$e(t)$	RTD function
$e(\theta)$	Normalized RTD function
F	tablet crushing force
FF316	spray dried lactose (fast flo 316)
ffc	flow function coefficient
ff_p	flow weighed for bulk density
ff_{rho}	flow weighed for density under consolidation
Methocel CR	K4M premium CR hydroxypropyl methylcellulose
Methocel DC2	K4M premium DC2 hydroxypropyl methylcellulose
HR	hausner ratio
IAR	immediate axial recovery
k	kinetic constant power law model
MgSt	magnesium stearate
M_t	amount of drug released at time t (power law model)
M_∞	amount of drug released after infinite time (power law model)
n	release exponent power law model
n_{tanks}	number of continuous stirred tank reactors
NAP	naproxen
NIRs	near infrared spectroscopy

p	plug-flow volume fraction
PLS	Partial Least Square
Pe	Péclet number
R ²	coefficient of determination
RMB	radial mixing blade
rpm	revolutions per minute
RSD	residual standard deviation
RSD _{Cout}	residual standard deviation on Cout of macro-mixing model
RSD _{cu}	residual standard deviation on tablet content
RSD _{wv}	residual standard deviation on tablet weight
RSD _{ss}	steady state blend uniformity, residual standard deviation predicted NAP content
RSD _{if}	short term blend uniformity, residual standard deviation in case of ideal feeding
RTD	residence time distribution
SiO ₂	fumed silica
Starch I500	partially pre-gelatinized starch
t _{20%}	time (h) to reach 20% drug release
t _{50%}	time (h) to reach 50% drug release
T	tablet thickness
t _m	mean residence time
t _{min}	minimum residence time or lag time
V _{screw}	volume dispensed per screw revolution
Q ²	goodness of prediction
ε _{powder}	powder porosity
ε _{tablet}	tablet porosity
ε _{fill}	screw flight fill fraction

ρ_{app}	apparent tablet density
ρ_{bulk}	bulk density
$\rho_{\text{consolidation}}$	density under consolidation
ρ_{screw}	density at the screw inlet
ρ_{tapped}	tapped density
ρ_{true}	true density
σ_{tm}^2	variance
σ_{\square}^2	normalized variance
Θ	dimensionless time
ω_{screw}	screw rotation rate

1 **I Introduction**

2 Interest in continuous processing is gaining momentum for pharmaceutical drug product manufacturing.
3 Although drug products are traditionally manufactured via a series of batch-wise unit operations (Engisch
4 and Muzzio, 2015), continuous processing offers several advantages to improve the manufacturing
5 efficiency of solid dosage forms: reduced costs through faster development and less scale-up, smaller
6 equipment footprint and elimination of intermediate storage (Vercruyssen et al., 2013). Implementation of
7 in-line process analyzers allows to monitor continuous processes which improves process understanding.
8 This enables the design of a process control and real-time-release strategy which should ultimately improve
9 the quality of the end product (Fonteyne et al., 2015; Simonaho et al., 2016).

10 Although direct compression is an inherently continuous technique, simple unit operations preceding
11 tableting (i.e. weighing and blending) are historically performed in batches. To enable continuous direct
12 compression, the integration of continuous powder feeding units, a continuous dry powder mixer and
13 tablet press is required. A handful of research papers recently described the feeding unit operation
14 (Cartwright et al., 2013; Engisch and Muzzio, 2014, 2012; W. E. Engisch and Muzzio, 2015; Meier et al.,
15 2016). Feeders can transfer problems of composition and flow rate variability to subsequent unit
16 operations when their flow rate variability is not well balanced with the amount of axial mixing within
17 the blender. Therefore, the ability to accurately dose a powder over time is a key challenge within the
18 overall manufacturing process. Continuous mixing studies previously focused on the influence of process
19 and design variables on the mixing efficiency and flow behavior within mixers (Pernenkil and Cooney,
20 2006). Multiple models are available in the literature to describe mixing and transport of particles through
21 a continuous mixer (Fogler, 2006). The main limitation of using residence time distribution (RTD) as a
22 predictive tool for mixing performance (Levenspiel, 1999) is its inability to capture micro-mixing. This is
23 especially important for pharmaceutical blending processes as they combine high product uniformity
24 requirements with small sample sizes. Studies correlating mixing performance with RTD suggested better
25 mixing performance when the RTD is broader (Gao et al., 2011) whilst other studies suggested the
26 performance is governed by the number of revolutions (Vanarase et al., 2010; Portillo et al., 2008). Due
27 to its importance in batch-wise processing, an impressive number of experimental and conceptual
28 compaction studies have been presented (Yu et al., 2014). Patel et al. (2006) underpinned the importance
29 of material properties and tableting speed on compressibility, tabletability and compactibility

30 This work is an extension of previous studies as experimental and/or conceptual knowledge was applied
31 to each unit operation of an integrated continuous direct compression process. Reports on
32 characterization of integrated from-powder-to-tablet continuous manufacturing platforms remain limited

33 (Ervasti et al., 2015; K. Järvinen et al., 2013; M. A. Järvinen et al., 2013; Simonaho et al., 2016; Vercruyssen
34 et al., 2013). Moreover, none of the described systems utilized an automated hopper refill system which is
35 a critical point within the manufacturing process (W. E. Engisch and Muzzio, 2015). Continuous direct
36 compression of an immediate release formulation was first reported by Järvinen et al. (2013). Tablets with
37 good mechanical properties were produced although pharmacopeial uniformity requirements were not
38 met under some conditions. The continuous manufacturing of extended release tablets via continuous
39 direct compression was up to now exclusively investigated by Ervasti et al. (2015). They mainly investigated
40 the impact of particle size (active and HPMC), drug load and mixer speed on product quality. HPMC
41 particle size was a critical material attribute as it impacted the quality attributes of sustained release tablets
42 such as weight variability and tablet strength (Ervasti et al., 2015). Tablet properties were more robust
43 when a better flowing HPMC was incorporated as hydrophilic matrix former although drug release
44 remained prone to mixer settings. Moreover, tablet quality showed significant variability over time as well
45 as within one grab sample. In addition, the mixing performance was not related to the powder flow
46 behavior within the mixer. Furthermore, a low system flow rate was selected (3.5 kg/h) throughout their
47 study. Clearly, significant challenges need to be overcome to enable continuous direct compression of
48 sustained release formulations. Among them, in depth characterization of the continuous mixing stage,
49 improving product quality and exploring the impact of operating at flow rates relevant for pharmaceutical
50 manufacturing.

51 This paper is organized as follows: the employed continuous direct compression manufacturing platform
52 is introduced in section 2. The used materials and applied methods are described in sections 3 and 4,
53 respectively. The obtained results are discussed in section 5. First, the properties of each material and
54 blend are elucidated (5.1). Second, the results of a fundamental loss-in-weight feeder characterization
55 procedure are interpreted (5.2). Third, an experimental design was conducted with HPMC CR grade to
56 understand the impact of impeller configuration and speed on process and product (5.3). Next, the impact
57 of drug load on the mixing performance was verified and related to the blend properties and consecutive
58 powder flow within the mixer and (5.4). Finally, the impact of HPMC grade and flow rate on was assessed
59 (5.5). Conclusions of this work are presented in section 6.

60 **2 Continuous direct compression equipment**

61 The CDC-50 (GEA APC Pharma Solids, Wommelgem, Belgium) combines material handling, loss-in-weight
62 feeding, two stage continuous blending, compression and in-line NIRs to monitor blend uniformity in an
63 integrated manufacturing system (figure 1).

64 The individual materials are transferred to dedicated top up systems through vacuum conveying or gravity.
65 The vacuum top up system consists of a conical hopper (3.2 L) with level sensor to regulate pneumatic
66 powder supply. The gravity feed system consists of a cylindrical feed tube and is used when powders
67 undergo triboelectric charging during vacuum transfer. Both systems are connected to a rotating top-up
68 valve (0.4, 0.8, 1.2 or 1.6 L) which allows consistent hopper refill of the screw feeder at optimal fill level.

69 Up to 6 GEA compact twin screw feeders can be integrated on the manufacturing system. The feeders can
70 be distributed over two feeding stations positioned at the inlet of the first and second continuous mixer
71 which holds a maximum of 6 and 2 feeders, respectively. The powder pump rests on top of the load cell
72 (2 kg range) and consists of a 2 L hopper connected with a twin screw feeding system. An impeller rotates
73 horizontally above the twin screws to ensure consistent screw flight filling and prevent bridging.

74 The blending process is conducted by two consecutive GEA continuous dry powder blenders which
75 separate the blending process into two distinct stages: the first blender is used for intensive mixing,
76 whereas shear-sensitive materials are introduced in the second blender. The GEA continuous dry powder
77 blender consists of a cylindrical processing chamber in which an impeller is rotating. The impeller is a shaft
78 which holds 60 mixing blades that have a fixed tolerance with the upwards tilted (15°) processing chamber.
79 Each blade can be positioned as a transport blade or a radial mixing blade (RMB) oriented respectively at
80 45° or 0° along the axis of the shaft. The mixer has a rotation rate that ranges from 45 to 450 rpm.

81 The blend is collected at the outlet of the second blender and guided via a borosilicate feed tube into the
82 feed frame of the tablet press (MODUL™ S, GEA APC Pharma Solids, Halle, Belgium). A level sensor
83 detects the fill level of the feed tube, which is maintained at its target during manufacturing by modulating
84 the turret speed via a proportional-integral-derivate controller. A fiber optic contact probe (Lighthouse™
85 probe, GEA APC Pharma Solids, Wommelgem, Belgium) is connected to an NIR spectrometer (Tidas P
86 analyzer, J&M Analytik, Essingen, Germany) and implemented in the feed tube just before the inlet of the
87 feed frame. Spectra are recorded every second during tablet production. The MODUL™ S is equipped
88 with moving rollers at the pre-compression station and fixed rollers at the main compression station.

89 **3 Materials**

90 Naproxen sodium was selected as a freely soluble cohesive model drug. The formulation contained 30%
91 w/w naproxen sodium ('NAP', Zhejiang Charioteer Pharmaceutical Company, Tongyuanxi, China), 30%
92 w/w hydroxypropyl methylcellulose (Methocel K4M premium CR, 'CR', Dow, Michigan, USA), 29% w/w
93 spray dried lactose (Fast Flo 316, 'FF316', Kerry, Naas, Ireland), 10% w/w partially pre-gelatinized starch
94 ('Starch 1500', Colorcon, Harleysville, USA), 0.5% w/w fumed silica (CAB-O-SIL M-5P, 'SiO₂', Cabot,

95 Amersfoort, The Netherlands) and 0.5% w/w magnesium stearate (Ligamed MF-2-V, 'MgSt', Peter Greven,
96 Venlo, The Netherlands). Methocel CR grade was compared to its Methocel DC2 equivalent to study the
97 impact of HPMC particle size and flow.

98 **4 Methods**

99 **4.1 Raw material characterization**

100 **4.1.1 Particle size distribution**

101 The particle size distribution of raw materials was measured in triplicate by laser diffraction (Mastersizer
102 S long bench, Malvern Instruments, Worcestershire, UK). The measurements were done via the dry
103 dispersion method in volumetric distribution mode using a 300 RF lens combined with a dry powder feeder
104 (Malvern Instruments, Malvern, UK) at a feeding rate of 3.0 G and a jet pressure of 2.0 bar. The particle
105 size distribution was analyzed via the Mastersizer 2000 software and reported as d10 and d50 values.

106 **4.1.2 Density and porosity**

107 The bulk (ρ_{bulk}) and tapped density (ρ_{tapped}) were determined in a 100 ml graduated cylinder (n=3) mounted
108 on a tapping device (J. Engelsmann, Ludwigshafen am Rhein, Germany). An exact mass of powder was
109 gently poured into the graduated cylinder. The initial volume and volume after 1250 taps were recorded
110 to calculate the bulk and tapped density, respectively. These values were used to calculate the Hausner
111 ratio (HR) and Compressibility index (CI):

$$112 \text{ Hausner ratio} = \frac{\text{Initial volume}}{\text{Volume after 1250 taps}} \quad (1)$$

$$113 \text{ Compressibility index (\%)} = 100 \times \frac{\text{Initial volume} - \text{Volume after 1250 taps}}{\text{Initial volume}} \quad (2)$$

114 The true density of all raw materials and blends were measured using helium pycnometry (AccuPyc 1330,
115 Micrometrics, Norcross, U.S.A.) at an equilibration rate of 0.0050 psig/min with the number of purges set
116 to 10. The powder porosity, $\varepsilon_{\text{powders}}$, was calculated (3) where ρ_{true} denotes true density (g/ml).

$$117 \varepsilon_{\text{powder}} = 1 - \frac{\rho_{\text{bulk}}}{\rho_{\text{true}}} \quad (3)$$

118 **4.1.3 Flowability of powders**

119 Powder flowability was measured in triplicate using a ring shear tester (Type RST-XS, Dietmar Schulze
 120 Schüttgutmesstechnik, Wolfenbuttel, Germany). The applied normal load at pre-shear was 1000 Pa,
 121 afterwards the powders were sheared under three different consolidation stresses: 400, 600 and 800 Pa.
 122 The density under consolidation at pre-shear ($\rho_{consolidation}$) was recorded. Powder cohesion (τ_c) was
 123 determined using the yield locus to estimate the shear stress at zero normal load. The flow function
 124 coefficient (ffc) was used to evaluate flowability. Furthermore, the density-weighted flow was calculated to
 125 assess the flow under gravity and expressed as ff_p (4) and ff_{rho} (5).

$$126 \quad ff_p = ffc \times \rho_{bulk} \quad (4)$$

$$127 \quad ff_{rho} = ffc \times \rho_{consolidation} \quad (5)$$

128 **4.2 Loss in weight feeding**

129 **4.2.1 Experimental set up**

130 The feeding behavior of materials included in this study was verified on the compact feeder (GEA,
 131 Wommelgem, Belgium). First, screws were primed prior to each run. Subsequently, the hopper was gently
 132 filled up to 2L. The corresponding weight (g) was recorded and considered as maximal. The hopper was
 133 run completely empty while the operation mode (volumetric or gravimetric), screw speed (rpm), net
 134 weight (g), feed factor (g/screw revolution) and feedrate (g/s) were logged every second. The drive
 135 command (%) was calculated by normalizing the screw speed with the max screw speed (462 rpm).

136 **4.2.2 Feed factor decay**

137 The volumetric feedrate (mL/s) of any screw feeder can be calculated (Engisch and Muzzio, 2014):

$$138 \quad \text{Volumetric feedrate} = V_{screw} \times \varepsilon_{fill} \times \omega_{screw} \quad (6)$$

139 Where V_{screw} (mL/revolution), ε_{fill} , ω_{screw} (revolutions/s) denote the volume dispensed per screw
 140 revolution, screw flight fill fraction and screw rotation rate, respectively. The volume dispensed per screw
 141 revolution is 4.86l or 2.40l mL for screws with a pitch of 20 or 10 mm, respectively. The fill fraction
 142 accounts for incomplete screw flight filling due to poor powder flow in the screw flights or screw layering.
 143 In order to calculate the gravimetric feed rate (g/s) one should multiply volumetric feedrate with the
 144 density (g/mL) of the material at the screw inlet, ρ_{screw} :

$$145 \quad \text{Gravimetric feedrate} = \rho_{screw} \times \text{volumetric feedrate} \quad (7)$$

146 At a fixed screw speed, the gravimetric feedrate over time (8) is solely related to the feed factor over time
 147 (9). If one assumes that ε_{fill} remains constant during steady state feeding, $\rho_{screw}(t)$ need to be determined
 148 in order to predict the gravimetric feedrate over time. Furthermore, a theoretical feed factor value is
 149 calculated by substituting ρ_{screw} with ρ_{bulk} in equation 9 and assuming complete screw flight filling. It was
 150 then evaluated if the theoretical feed factor provides a good estimate of the actual value.

$$151 \text{ Gravimetric feedrate } (t) = \text{feed factor } (t) \times \omega_{screw} \quad (8)$$

$$152 \text{ Feed factor } (t) = \rho_{screw}(t) \times V_{screw} \times \varepsilon_{fill} \quad (9)$$

153 The feed factor versus weight profiles, further referred to as feed factor profiles, indicate the feed factor
 154 and hence also the density at screw inlet decay with a decreasing net weight in the hopper. To compare
 155 the feeding behavior of materials with different density, the variable hopper fill level (10) is introduced to
 156 normalize the net hopper weight for the maximum weight in the hopper. The maximum feed factor is
 157 typically observed at higher fill levels where the feed factor remains relatively stable. It can be used to
 158 estimate the feeding capacity for a particular material. Normalized feed factor profiles were constructed
 159 by normalizing the feed factor for the maximum feed factor (11). These normalized feed factor profiles
 160 allow to study the shape of the feed factor decay in case of absolute differences in the maximum feed
 161 factor. Hence normalized feed factor profiles allow to define a minimum fill level and select a suitable refill
 162 regime for each material.

$$163 \text{ Fill level } (t) = \frac{\text{Net weight } (t)}{\text{Maximum weight}} \times 100 \quad (10)$$

$$164 \text{ Normalized feed factor } (t) = \frac{\text{feed factor}(t)}{\text{Maximum feed factor}} \times 100 \quad (11)$$

165 **4.3 Continuous blending**

166 **4.3.1 Experimental set-up**

167 At the first blending stage, the impact of impeller rotation rate and configuration was investigated according
 168 to a full factorial design of experiments where each factor was tested at three levels. The impeller
 169 configuration (figure 2) was considered as a quantitative factor by extending the shear zone in the middle
 170 of the impeller with RMB (8, 12 or 16). The impeller speed was set at 200, 300 and 400 rpm for each
 171 impeller configuration. The flow rate (25 kg/h), second blender settings and formulation (CR grade)
 172 remained fixed during this experimental design. The investigated responses were flow behavior within the
 173 continuous mixer (fill level, strain, RTD analysis and modeling), mixing performance (BU) and tablet quality

174 (content uniformity and weight variation). Additional experiments were performed to evaluate the impact
175 of HPMC grade. Finally, the feasibility of operating at high flow rates (50 and 75 kg/h) was explored for
176 the better flowing Methocel DC2-based formulation. For these trials tablet quality characterization was
177 extended with tensile strength and dissolution.

178 **4.3.2 Development and verification of NIR blend uniformity models**

179 NIR-based Partial Least Square (PLS) regression models were constructed during in-line monitoring of
180 NAP content. Data analysis was performed using SIMCA 14 (Umetrics AB, Umeå, Sweden). The PLS
181 models were developed by regressing 2750 (11 calibration standards x 250 spectra/standard) inline
182 collected and pre-processed NIR spectra with their corresponding concentration of NAP. Spectra were
183 collected in the spectral region from 1091 to 2107 nm with a pixel dispersion of 3.97 nm. Each
184 spectrum was collected with an integration time of 60 ms and averaged over seven scans such that
185 NIRs samples approximated the weight of unit dose (i.e. 400 mg). Spectra were recorded every second.
186 The verification set consisted of 11 independent verification standards which each contained 50 spectra.
187 At nominal concentration (30.5 %), three independent calibration and verification runs were performed.
188 The NAP level of each standard is depicted in table 3.

189 Two spectral regions specific for NAP were selected for analysis (1130-1230 and 1404-1739 nm). These
190 spectral regions were standard normal variate corrected and mean-centered before PLS was performed.
191 Three PLS components were chosen as the goodness of prediction of the model did not significantly
192 improved ($Q^2 = 0.99$) when adding extra components. The scores and loading plot of the first component
193 confirmed this component represents the variation in NIR spectra caused by the difference in NAP
194 concentration. Positive peaks in the loading of the first component corresponds to spectral peaks of NAP
195 which confirmed thereby the specificity of the method. A higher score for component 1 therefore indicates
196 a higher NAP concentration.

197 Standard cross-validation was applied by dividing the dataset in 7 groups. The root mean squared error of
198 cross validation of this three component PLS model was 0.52 % (w/w). The predictive performance of this
199 model was subsequently evaluated by predicting the concentration for all verification standards (table 3).
200 This resulted in an overall root mean squared error of prediction value of 0.51% (w/w). A linear relation
201 between target concentration and model predicted concentration was found ($R^2 = 0.99$).

202 **4.3.3 RTD estimation and analysis**

203 The RTD was estimated by performing an impulse response test: a pulse of NAP was introduced at the
 204 inlet of the first blender whilst its concentration was monitored via in-line NIRs as a function of time at
 205 the system outlet (feed tube of the tablet press). The response is the concentration as a function of time
 206 (s), i.e. the concentration profile $c(t)$. The amount of tracer (max 25 g) was selected such that the system
 207 response was detectable with near infrared spectroscopy and within the calibrated range (section 4.3.2).
 208 Furthermore, the pulse size was limited to ensure the steady state of the process was not disturbed. The
 209 $c(t)$ curve was used to calculate the RTD function $e(t)$ with equation (12). Note that $e(t)$ normalizes the
 210 concentration profile $c(t)$ by the total amount of tracer $\int_0^\infty c(t)dt$.

$$211 \quad e(t) = \frac{c(t)}{\int_0^\infty c(t)dt} \quad (12)$$

212 The RTD function $e(t)$ and mean residence time (t_m) were used to obtain the normalized residence time
 213 which is calculated as $e(\theta) = e(t) \times t_m$ and where θ is the dimensionless time, i.e. $\theta = \frac{t}{t_m}$. The variance
 214 (σ_{tm}^2) and normalized variance (σ_θ^2) are measures of the spread of the RTD and normalized RTD curve,
 215 respectively. The RTDs were quantitatively assessed by calculating t_m , σ_{tm}^2 and σ_θ^2 (equation 13 – 15)
 216 (Fogler, 2006). By treating the boundary condition of the mixer as a closed system with no axial or radial
 217 variation in upstream and downstream concentrations to axial dispersion model, Péclet number (Pe) was
 218 calculated using equation 16 (Kumar et al., 2014). The dimensionless Péclet number is the ratio of the rate
 219 of convection and dispersion. Further interpretation of these RTD measures is described in section 5.3.1.

$$220 \quad t_m = \frac{\int_0^\infty t \cdot e(t)dt}{\int_0^\infty e(t)dt} \quad (13)$$

$$221 \quad \sigma_{tm}^2 = \frac{\int_0^\infty (t-t_m)^2 \cdot e(t)dt}{\int_0^\infty e(t)dt} \quad (14)$$

$$222 \quad \sigma_\theta^2 = \frac{\sigma_{tm}^2}{t_m^2} \quad (15)$$

$$223 \quad \frac{\sigma_{tm}^2}{t_m^2} \approx \frac{2Pe-2+2 \cdot e^{-Pe}}{Pe^2} \quad (16)$$

224 4.3.4 RTD Modeling

225 A non-ideal flow model has been used to describe the powder flow inside the continuous mixer: the tanks
 226 in series model with plug-flow volume fraction was selected to fit the normalized RTDs, $e(\theta)$. The model
 227 (17) is a three parameter flow model (Levenspiel, 1999).

228
$$e(\theta) = \frac{b[b(\theta-p)]^{n-1}}{(n-1)!} \exp[-b(\theta-p)] \quad (17)$$

229 Where $n = n_{tanks} = \text{number of continuous stirred tank reactors}$, $p = \frac{t_{min}}{t_m}$ and $b = \frac{n}{1-p}$ (18)

230 Where t_{min} is the minimum residence time and p is the volume fraction of the continuous mixer that is
 231 assumed to correspond to plug-flow. The parameters defining $e(\theta)$ are the number of tanks in series and
 232 the minimum and mean residence time. The mean residence time was calculated (13) whereas the number
 233 of tanks and minimum residence time were estimated by minimizing the residual sum of squares (19)
 234 between experimental and fitted data as described by Kumar et al. (2015). The coefficient of determination
 235 (R^2) was used to assess model performance.

236
$$\text{Residual sum of squares} = \sum (e(\theta)_{exp} - e(\theta)_{sim})^2 \quad (19)$$

237 One can calculate the fitted RTD using the fitted normalized RTD, $\frac{e(\theta)}{t_m} = e(t)$ (20)

238 4.3.5 Model based macro-mixing evaluation

239 Axial mixing describes the transport and back mixing in the system and is characterized by estimating the
 240 RTD. The design and process variables of the continuous blender must be carefully selected such that its
 241 RTD has sufficient macro-mixing ability to filter out feeder fluctuations. Levenspiel (1999) illustrated one
 242 can predict the concentration of the active in the outlet stream of a continuous mixer $C_{out}(t)$. Therefore,
 243 the fitted RTD and concentration of the active in the inlet stream (C_{in}) have to be determined using
 244 equations 20 and 21, respectively. Subsequently, these signals were convoluted (22) in Matlab R2015b
 245 (Mathworks, Natick, Massachusetts, USA).

246
$$C_{in}(t) = \frac{FR_{NAP+SiO_2}(t)}{FR_{NAP+SiO_2}(t) + FR_{FF316}(t) + FR_{HPMC}(t) + FR_{Starch}(t) + FR_{MgSt}(t)} \times 100 \quad (21)$$

247 Where $FR(t)$ is the gravimetric flow rate over time for the component specified.

248
$$C_{out}(t) = \int_0^t C_{in}(t-t') E(t') dt' = \int_0^t C_{in}(t') E(t-t') dt' \quad (22)$$

249 The residual standard deviation on the tracer concentration in the outlet stream (RSD_{Cout}) was
 250 determined as an indicator of macro-mixing performance.

251 4.3.6 Fill level measurement

252 The fill level or residence mass is defined as the amount of material in the mixer. During start-up, the fill
253 level increases with time before a plateau is reached. The mixer operating under constant fill level is
254 considered to be operating at steady state conditions. The fill level in the mixer determines the residence
255 time and thus the strain experienced by the powder inside the mixer. The fill level in the blender was
256 determined by stopping the steady state process instantaneously. The powder inside the blender was then
257 collected pneumatically. In the absence of dead volumes inside the continuous mixer, fill level measurement
258 is complementary to mean residence time calculation from RTD estimation (Vanarase and Muzzio, 2011).

$$259 \text{ Bulk residence time (s)} = \frac{\text{Fill level (g)}}{\text{Flow rate } \left(\frac{\text{g}}{\text{s}}\right)} \quad (23)$$

260 4.3.7 Strain measurement

261 In convective continuous mixers, energy input is provided by the rotating impeller. The impeller speed
262 influences the fill level and mean residence time. Strain is thereby proportional to the product of speed
263 and mean residence time which reflects the number of blade passes in the mixer (Vanarase et al., 2013b).

$$264 \text{ Number of blade passes} = \text{Mean residence time (s)} * \frac{\text{Impeller speed (rpm)}}{60} \quad (24)$$

265 4.4 Tableting

266 4.4.1 Experimental set-up

267 The Modul S press was equipped with an overfill cam of 14 mm and 38 punches (euro B, 10 mm diameter,
268 concave) to produce tablets with a target weight of 400 mg. The press operated in an automatic mode
269 where the pre-compression displacement signal was used to monitor tablet weight which was controlled
270 by adjusting fill depth. The standard paddles were installed in the forced feeder and their speeds were kept
271 constant at 30 and 60 rpm for the first and second paddle feeder, respectively. The turret speed was set
272 to ensure that the theoretical flow rate of the press matched the total flow rate of the feeders. This
273 corresponded to a speed of 27, 55 and 82 rpm for a flow rate of 25, 50 and 75 kg/h, respectively. During
274 start-up the feed tube level initiated turret rotation at its target (50%). The turret speed was modulated
275 during processing to maintain this target. Below 20% feed tube level, the press was stopped to allow filling
276 of the feed tube, whereas at 100% feed tube level the mixer and feeders were stopped. Pre-compression
277 force was set at 15.2 MPa. The pre-compression height, i.e. the distance between the punches at pre-
278 compression, was regulated with 0.01 mm adjustments such that a minimal pre-compression displacement
279 of 0.1 mm at the rollers was maintained. The main compaction height was set at 2.252 mm whilst the main
280 compression pressure was monitored. At each flow rate, tableting, compressibility and compactibility

281 profiles were constructed by tableting at a main compaction pressure of 127, 190, 229, 254, 318 and 381
282 MPa.

283 **4.4.2 Tablet characterization**

284 **4.4.2.1 Weight variability**

285 Tablets (n=10) were randomly selected from grab samples collected at an interval of 10 s. Tablet weight
286 variability was expressed as the residual standard deviation on the tablet weight (RSD_{wv}).

287 **4.4.2.2 Tablet strength and porosity**

288 Tablets (n=20) were weighed and their hardness, thickness and diameter was determined (Sotax HT 10,
289 Basel, Switzerland). The tablet tensile strength (MPa) was calculated using equation 25 where F, d and T
290 denote the crushing force (N), tablet diameter (mm) and tablet thickness (mm), respectively.

$$291 \text{ Tensile strength} = \frac{2F}{\pi dT} \quad (25)$$

292 The porosity of the formed compacts was calculated using equation 26 where ρ_{app} denotes the apparent
293 tablet density (g/mL) which was calculated by dividing the tablet mass by its volume.

$$294 \varepsilon_{\text{Tablet}} = 1 - \frac{\rho_{app}}{\rho_{true}} \quad (26)$$

295 **4.4.2.3 Immediate axial recovery (IAR)**

296 Axial recovery of tablets after ejection was calculated via equation 27 (Armstrong and Haines-Nutt, 1972):

$$297 \text{ Immediate axial recovery \%} = \frac{\text{tablet height}_{\text{after ejection}} - \text{tablet height}_{\text{under main compression}}}{\text{tablet height}_{\text{under main compression}}} \times 100 \quad (27)$$

298 **4.4.2.4 Content uniformity**

299 Tablets (n=30) were randomly selected from a grab sample collected during steady state processing. Each
300 tablet was homogenized in 400 mL phosphate buffer with a pH of 7.4 (USP monograph) using an automated
301 tablet preparation workstation (TPW™, Sotax, Basel, Switzerland). Subsequently, 10.0 mL of homogenate
302 was filtered and the NAP content derived from the absorbance of the filtrate at 332 nm using a UV
303 spectrophotometer with 0.5 cm cell (Agilent 8453, Agilent technologies, Santa Clara, USA). Content
304 uniformity (CU) was expressed as the residual standard deviation on the NAP content (RSD_{cu}).

305 **4.4.2.5 Dissolution**

306 Dissolution tests were performed (n=6) in pH 7.4 phosphate buffer using the paddle method with sinkers
307 (USP monograph for NAP tablets). The temperature of the dissolution medium was maintained at 37 ±

308 0.5 °C, while the rotation speed was set at 100 rpm. Samples of 9 mL were withdrawn after 0.5, 1, 2, 4, 6,
309 8, 10, 12 and 16 h. The drug content in these samples was derived from the absorbance of the samples at
310 332 nm using a UV spectrophotometer (1 cm cells).

311 The percent drug released versus time profiles were used to investigate the mechanism of drug release
312 and evaluate the influence of process settings. The power law was used as a simple semi-empirical equation
313 (28) to describe the drug release from the polymeric systems (Siepmann and Peppas, 2012):

$$314 \frac{M_t}{M_\infty} = kt^n \quad (28)$$

315 Where, M_t is the amount of drug released at time t , M_∞ is the amount of drug released after infinite time,
316 k is a kinetic constant incorporating structural and geometric characteristics of the tablet, and n is the
317 release exponent, indicative for the drug release mechanism. The model was fitted using the curve fitting
318 toolbox in Matlab R2015b. For matrix tablets, a release exponent of 0.5 indicates diffusion-controlled drug
319 release whereas 1.0 indicates erosion or swelling-controlled release. Intermediate values suggest that
320 diffusion and erosion contribute to the overall release mechanism (Levina and Rajabi-Siahboomi, 2004;
321 Siepmann and Peppas, 2012). The time to reach 20% and 50% release were also included as responses.

322 **5 Results and discussion**

323 **5.1 Raw material characterization**

324 Individual materials and blends were characterized extensively to compile a multivariate dataset
325 (complementary data). Subsequently, principal component analysis was applied on this dataset (SIMCA 14).
326 The score plot was used (figure 3, left) to identify how individual materials and blends are situated with
327 respect to each other whereas the loading plot (figure 3, right) was used to reveal how variables are related
328 to each other. The score and loading plots were observed simultaneously to reveal the physical meaning
329 of these components. Materials with a specific location on the score plot have high values for variables
330 with similar position on the loading plot (positively correlated) and low values for variables at the opposite
331 side of the loading plot (negatively correlated). To evaluate a variable, one can draw a straight line through
332 the origin and project other variables of interest on that line to assess their correlation. Additionally, the
333 correlation matrix (complementary data) was used to verify their magnitude of correlation.

334 Three components were fitted in the model explaining 96 % of the variation in the dataset. The first,
335 second and third component explained 74, 16 and 6 %, respectively. The first component corresponds to
336 density-weighted flow as these variables have high positive loadings for the first component but relatively

337 low loadings for the second component. Materials with high scores for component 1 flow well under
338 gravity and usually consist of larger particles. Furthermore, the different densities are correlated as they
339 cluster in the right top corner and are negatively correlated with porosity which is located in the left
340 bottom corner. Powder flow and fines are positioned in the right bottom corner of the loading plot (figure
341 3, right) and are negatively correlated with cohesion (left top corner). Powder flow deteriorated when the
342 powder bed contained more fine particles due to their high cohesiveness. The variation in the dataset for
343 density, flow, cohesion and porosity is clearly described by the second principal component. However,
344 there is no single property which truly describes this second component as these variables are not
345 completely independent from the first component (i.e. density-weighted flow). The variability in
346 compressibility and cohesion of the powder bed is described by component 3 (not shown).

347 The key properties of each individual material are depicted in table 1. The score plot reveals Starch 1500
348 is situated in the top right corner: the powder combined easy flow with high density and flowed as a
349 consequence well under gravity. Spray dried lactose (FF316) combined better flow with similar density
350 which explains why its density-weighted flow was even higher. FF316 had a remarkably lower tapped density
351 (0.71 g/mL) compared to Starch 1500 (0.80 g/mL) and has therefore lower scores for component 2. MgSt
352 is situated in the left bottom corner of the score plot due to its poor density-weighted flow ($ff_p = 0.42$)
353 combined with its specifically low true density (1.04 g/mL) and high porosity (0.82). Compared to MgSt,
354 NAP is situated slightly more to the right side but significantly higher along the axis of component 2. NAP
355 flows also poor under gravity ($ff_p = 0.34$) but is significantly denser. Pre-blending NAP with SiO₂ improved
356 powder flow although SiO₂ made the powder bed more compressible. Both HPMC grades had a unique
357 location on the score plot: low positive scores for component 1 and high negative scores for component
358 2. The HPMCs combine easy flow with relatively low density. The Methocel DC2 grade was plotted to the
359 right of Methocel CR grade. The direct compression grade has a higher particle size which improves
360 powder flow and reduces the cohesiveness and compressibility of the powder bed.

361 Two placebo sustained release platform formulations (section 3), composed of either Methocel CR or
362 Methocel DC2 as matrix former, were characterized to evaluate the impact of HPMC grade on blend
363 properties. The Methocel DC2 blend was positioned to the right of the Methocel CR blend on the score
364 plot. This was attributed to the improved flow (flow function coefficient of 6.80 compared to 5.75) and
365 slightly higher bulk density (0.46 vs 0.44 g/mL) of the Methocel DC2 blend. Both placebo blends shifted to
366 the left on the score plot when 30% NAP was incorporated in the formulations. The high level of NAP
367 reduced the density and deteriorated the flow. However, the Methocel DC2-based blend clearly retained
368 the most favorable blend properties as it had higher scores for component 1 and 2. The score plot also
369 revealed the impact of drug load on blend properties. An increase in NAP content gradually reduced the

370 density and deteriorated the flow: a drug load increase from 21 to 40% reduced the flow function
371 coefficient from 2.15 to 1.53 and the bulk density from 0.41 to 0.29 g/mL.

372 This principal component model functions as a dynamic raw material property database that reveals in
373 which properties materials differ. Loading new samples in the model allows to situate them among
374 materials for which process knowledge is already established. Moreover, characterizing materials enabled
375 correlation and modeling of their properties with process and product responses. In other words the key
376 material properties at the loss-in-weight feeding (section 5.2), continuous blending (section 5.4 and 5.5)
377 and tableting (section 5.5.2) unit operation could be revealed.

378 **5.2 Loss-in-weight feeding**

379 All feed factor profiles showed a similar trend: the feed factor was initially near its maximum when the
380 hopper of the feeder was completely full (Figure 4). The feed factor remained then relatively stable during
381 emptying until a material specific hopper fill level was reached. Subsequently the feed factor decreased
382 gradually towards a minimal feed factor (figure 4, left). One can assume that the actual weight of the
383 powder bed regulates the compression of powder at the screw inlet over time. The powder bed is
384 densified as a function of the gravitational pressure exerted by its own weight. Hence the compressive
385 pressure decreased when feeders emptied their hopper. The resulting decrease in density at the screw
386 inlet is hypothesized to cause this feed factor decay.

387 The maximum feed factor was correlated with bulk density ($R^2 = 0.85$) (figure 4, right). Twin screws act as
388 a pump by displacing a fixed volume, i.e. the volumetric feed factor, every screw revolution. Therefore, a
389 higher density at the screw inlet yields theoretically a higher feed factor. This theoretically predicted feed
390 factor-bulk density relation (calculations and assumptions described in section 4.2.2) corresponds relatively
391 well with the experimentally derived feed factor-bulk density relation. However, flow properties clearly
392 confounded the bulk density-feed factor correlation. Two materials deviated from the theoretical curve
393 which indicated that bulk density is not the only property governing the transport capacity. NAP is classified
394 as a very cohesive material and has a significantly lower feed factor compared to slightly better flowing
395 materials with similar density (i.e. NAP+SiO₂). This might be attributed due to screw layering and/or
396 incomplete screw flight filling by NAP. In contrast, the experimentally derived feed factor of the freely
397 flowing FF316 was lower than the theoretically predicted feed factor. As incomplete screw filling seems
398 unlikely for FF316, the density in the screw inlet must have been significantly lower than the bulk density.
399 It is hypothesized the powder was loosely packed in the screw because the particles flowed freely in the
400 rotating screw instead of being transported as a packed bed. Interestingly, the maximum feed factor for
401 Starch 1500 (2.97) was significantly higher compared to FF316 (2.12). Both materials have a similar bulk

402 density (≈ 0.63 g/mL) but packed significantly different (i.e. Starch 1500 has a Hauser ratio of 1.29 compared
403 to 1.13 for FF316) and flowability (i.e. Starch 1500 flow is passable and FF316 flow is good). Due to its
404 compressibility, Starch 1500 has the ability to densify in the hopper and/or screw. In combination with its
405 moderate flow properties, Starch 1500 will be efficiently transported as a packed bed instead of loose
406 particles. Furthermore tapped density, compared to bulk density, generally correlated better with the
407 maximum feed factor ($R^2 = 0.91$). These observations underpinned that bulk density, compressibility and
408 powder flow impact the maximum feed factor value.

409 Table 2 presents the feeder flow rate ranges based on a system flow rate range of 25 to 75 kg/h and the
410 ratio of the components in the formulation. The maximum feed factor value was used to estimate the drive
411 command at the intended flow rates. Twin concave screws with 20 mm pitch appeared to be perfectly
412 suited to dose the high throughput products FF316 and Methocel DC2. Due to its high feed factor, a
413 relatively low drive command (3.0 %) was required to dose Starch 1500 at 2.5 kg/h. The feeder was
414 therefore equipped with 10 mm pitch concave screws to enable operation at double the drive command
415 (6.1%) and avoid thereby pulsating mass flow. Due to its low dose in the formulation, MgSt required an
416 extremely low mass flow (0.125 kg/h) which inevitably resulted in an extremely low drive command (0.5
417 %) using concave screws with 20 mm pitch. Hence, screws with 10 mm pitch were selected to enable MgSt
418 dosing at higher drive command (1.3 %). A single feeder dosing pure NAP was not able to achieve the
419 maximum flow rate of 22.5 kg/h. One strategy could be to set-up multiple NAP feeders in parallel.
420 Alternatively, feeding a NAP+SiO₂ pre-blend at the maximum flow rate (22.9 kg/h) required 76.4% drive
421 command. During in-line blending trials at 75 kg/h two NAP+SiO₂ feeders were eventually installed to
422 prevent operating near the drive command limits at lower hopper fill levels.

423 A hopper refill strategy was derived from the normalized feed factor profiles (figure 4, middle). The goal
424 is to operate the feeder within a fill level window where the feed factor remains stable and close to its
425 maximum value. Hence, less control actions are required to deal with feed factor kinetics during emptying
426 and refilling of the hopper. The feed factor remained relatively stable till low fill levels for Starch 1500,
427 FF316 and HPMC: a feed factor decrease of 5% was only observed below 15 % fill level. Their feeders were
428 therefore run down to 20% fill level before triggering a refill. Highly compressible powders with low density
429 displayed a decay at significantly higher fill level. A decay of 5% was already reached at 80, 50 and 20% fill
430 level for NAP, MgSt and NAP+SiO₂, respectively. The normalized feed factor profile clearly illustrated an
431 additional advantage of dosing NAP+SiO₂ pre-blend: the normalized feed factor remained constant till 40%
432 fill level for the pre-blend whereas the decay was initiated from the start for NAP. A refill at 40% fill level
433 was triggered for the pre-blend and MgSt. Operating in the same feed factor window with NAP would

434 require more frequent refills. The actual impact of hopper refills during continuous manufacturing was
435 further investigated at the feeding and blending unit operation (section 5.3.6).

436 **5.3 Effect of impeller configuration and speed**

437 Residence time estimation was performed as a function of impeller speed (i.e. RPM) and configuration (i.e.
438 RMB) (figure 5). Besides changes in RTD profiles, the impact of process and design parameters was clearly
439 reflected in other process and product responses. Therefore, a PLS model was fit, simultaneously
440 representing the variation of all responses to the variation and interaction of the factors. Thereby the
441 loading plot is a useful tool to understand how factors and responses are correlated (figure 6). The loading
442 plot shows that the first PLS component is dominated by the number of RMB mounted on the impeller
443 (on the negative side of the X-axis) and to a lesser extent by impeller speed (on the positive side). The
444 second component is a combination of impeller speed and the quadratic and interaction model terms.
445 Several responses appear to be correlated: the spread of the (normalized) RTD, fill level, strain, bulk and
446 mean residence time cluster along the axis of component 1 on the loading plot. These responses have
447 higher values when the impeller is equipped with more RMB and operates at lower speed. Responses
448 describing the ratio of convective transport and dispersive mixing (péclet number and number of tanks)
449 showed negative correlation with this response cluster, especially with the normalized variance. Installing
450 more RMB and lowering the mixing speed improved the axial mixing efficiency (low number of péclet and
451 tanks and low variability in the outlet stream). Remarkably, the blend uniformity measures are located near
452 the origin and hence not significantly impacted by the investigated factors. Variability in tablet weight and
453 content was higher for high values of the second component indicating the importance of the quadratic
454 terms to describe their variance. Remarkably, these tablet properties did not group with RTD related
455 responses. Hence one can conclude that both RTD estimation and product quality determination were
456 required to fully characterize the manufacturing system. Effects and factor interactions are discussed in
457 more detail below using figures 7, 8, 9 and 10. The size of the effect is presented in a table below the
458 corresponding effect plot.

459 **5.3.1 Powder flow behavior in the continuous mixer**

460 **5.3.1.1 Effect on fill level, bulk residence time and mean residence time**

461 The responses fill level, bulk residence time and mean residence time spanned a wide range from 0.096 to
462 0.610 kg, 24 to 88 s and 97 to 196 s, respectively. Overall, good correlation ($R^2=0.96$) was observed
463 between the responses bulk residence time and mean residence time, indicating that fill level measurements
464 and RTD estimations are complementary. The NIRs probe is implemented in the feed tube of the tablet
465 press which explains the absolute difference between bulk and mean residence time. The impeller

466 configuration is an important factor to include in RTD studies for continuous mixers as the impeller drives
467 the mixing and transport of particles through the mixer. The RMB had a significant effect on fill level, bulk
468 and mean residence time (figure 7, top). By extending the RMB section, more powder accumulated in the
469 mixer due to more restricted material flow. For fill level and bulk residence time, this effect was not linear
470 and intensified when more RMB were installed. The experimental error inherently associated with RTD
471 estimation (higher error bars compared to fill level estimation) probably caused statistical insignificance of
472 the quadratic term for mean residence time. Next to the number of RMB, the main effect of impeller speed
473 was significant for fill level, bulk and mean residence time. This can be explained by the higher conveying
474 rate of powder within the blender when the impeller rotates faster. The impact of speed on fill level and
475 bulk residence time was mainly linear as the quadratic term had a statistically significant although very
476 limited effect. The interaction effect (figure 7, bottom) of RMB and speed on fill level, bulk and mean
477 residence time was significant. Remarkably, an increase in speed reduced the impact of the impeller
478 configuration. At low filling conditions (i.e. for low number of RMB), marginal differences in these responses
479 were observed when the impeller speed was varied from its low to high level. For this configuration, the
480 conveying rate at low impeller speed was still sufficiently high to prevent an accumulation of powder in the
481 mixing section. When the length of the mixing section is extended and the mixer operates at low speed,
482 the powder transported by the initial conveying section is less able to pass the mixing section without
483 undergoing restriction to flow. Consequently, the powder accumulates in the mixer under these
484 conditions. Operating at high impeller speed level increased the conveying rate which reduced the
485 efficiency of the shear zone to restrict powder flow. Consequently fill level, bulk and mean residence time
486 were more reduced (figure 7).

487 **5.3.1.2 Effect on minimum residence time**

488 The lag time describes the rate of transport through the blender. Quantifying the minimum residence time
489 is important to understand when disturbances at the feeding stage will reach the inlet of the tablet press.
490 The minimum residence ranged from 7 to 53 s. The effect plot shows the main effects of impeller speed
491 and number of RMB are statistically significant in contrast to their quadratic and interaction terms (figure
492 7, top). Remarkably, the minimum residence time is the only response where speed is the most influential
493 factor. The enhanced conveying rate reduced transport time through the blender. In contrast, equipping
494 the impeller with more RMB restricted powder flow which slowed down the transport rate.

495 **5.3.1.3 Effect on Normalized variance**

496 Perfectly mixed-flow is described by a continuously stirred tank reactor and for such a system the spread
497 of the normalized RTD curve is equal to one. By contrast, a plug-flow reactor describes a perfectly unmixed
498 system and under this condition the normalized variance is equal to zero (Fogler, 2006). A higher

499 normalized variance indicates better axial mixing conditions. In our study, the impeller configuration and
500 speed significantly affected the normalized variance (figure 8, top) which ranged from 0.04 to 0.18 and
501 suggests the flow behavior in the blender was in between mixed and plug-flow. Extending the mixing section
502 on the impeller from 8 to 16 RMB yielded a higher normalized variance which indicates the RMBs induced
503 dispersion. Changing speed from 200 to 400 rpm reduced the spread of the normalized RTD indicating
504 less dispersion occurred at higher conveying rate. The data suggest a linear effect of impeller configuration
505 and speed as the quadratic and interaction terms were not statistically significant and limited in size (figure
506 8, top). Hence the normalized RTD can be widened by combining a low impeller speed with high number
507 of RMB (figure 8, bottom).

508 **5.3.1.4 Effect on Péclet number, number of tanks and plug-flow volume fraction**

509 As the spread of the RTD curve approaches zero, the péclet number approaches infinity indicating the
510 extent of axial mixing is low and the mixer characteristics approach a plug-flow reactor. This regime is not
511 favorable for continuous processing as plug-flow corresponds to low axial mixing efficiency which can
512 result in poor dampening of instream fluctuations (Kumar et al., 2014). The applied normalized RTD model
513 (section 4.3.4) contained two physically significant parameters namely the plug-flow volume fraction and
514 number of constantly stirred tank reactors in series. These allow the quantification of the plug-flow volume
515 fraction and axial mixing efficiency, respectively. Less tanks in series corresponds to more efficient axial
516 mixing. Figure 5 confirms good model fit was achieved using the RTD model presented in section 4.3.4 (R^2
517 = 0.95-0.99).

518 Impeller configuration and speed had a significant impact on axial mixing efficiency (figure 8, top). Within
519 this investigation the number of péclet and tanks ranged from 10 to 47 and 2 to 18, respectively. In contrast,
520 these factors had no significant impact on the plug-flow volume fraction which indicates the impeller
521 configuration had a similar impact on the minimum and mean residence time (figure 7, top). The impeller
522 configuration had the largest impact on the axial mixing efficiency. By extending the impeller configuration
523 with RMB, the powder undergoes relatively more dispersion than transport within the mixer. In contrast,
524 the main effect of impeller speed is a higher péclet number and more tanks in series. Higher speed yields
525 higher conveying rates which results in less axial mixing and more plug-flow like material transport through
526 the mixer. A strong interaction occurred between impeller configuration and speed for the péclet number
527 and amount of tanks in series (figure 8, bottom). Processing conditions which resulted in high blender fill
528 levels increased the axial mixing efficiency. When the impeller is equipped with low number of RMB, axial
529 mixing is only effective at low speed as material flow is then restricted in the mixing section more
530 frequently. An impeller with high number of RMB subjected particles to a critical strain and homogenization

531 force making speed less influential for the efficiency of axial mixing. Hence equipping the impeller with high
532 number of RMB is a powerful tool to maintain optimal dispersion at high impeller speed.

533 **5.3.2 Strain**

534 The strain or number of blade passes experienced by the powder within the continuous mixer was clearly
535 dominated by the impeller configuration (figure 9, top). Significantly more strain was applied on the powder
536 when the number of RMB was varied from low to high. The quadratic term had a significant albeit small
537 positive effect, indicating that extending the shear zone with more RMB gradually resulted in more blade
538 passes. The increase in strain originates from a significant change in bulk residence time associated with
539 higher number of RMB (section 5.3.1.1 and figure 7, top). Next to impeller configuration, the main effect
540 of impeller speed and its quadratic term had a negative impact on the applied strain (figure 9, top). In
541 general, the number of blade passes was maximal at intermediate impeller speed (figure 9, bottom). This
542 was previously reported by other researchers for different continuous mixers and formulations (Vanarase
543 and Muzzio, 2011; Vanarase et al., 2013). However, an interaction occurred when a high number of RMB
544 was combined with low impeller speed, yielding similar blade passes compared to intermediate speed
545 (figure 9, bottom). This observation can be explained by the interaction plot of bulk residence time (figure
546 7, bottom). At low speed and high number of RMB, the maximized bulk residence time compensates for
547 the lower speed and yields similar blade passes.

548 **5.3.3 Blend Uniformity**

549 Section 5.3.1 described the macroscopic powder flow behavior within the continuous mixer. However,
550 these RTDs do not capture the mixing performance. Therefore, the mixing process was monitored using
551 in-line NIRs to determine the homogeneity of the blend stream from the mixer. The relative standard
552 deviation on the content of NAP in the blend during steady state processing was calculated as a mixing
553 index (RSD_{ss}) and accounts for variability on the long and short term. Imperfections in the feed rate can
554 introduce variability on the long term. By contrast, micro-mixing performance refers specifically to the
555 extent of de-agglomeration and local segregation and is expressed as the NAP variability over a short time
556 interval (RSD_{if}). This corresponds to the remaining variability in the case of ideal feeding performance (Gao
557 et al., 2011) which can be due to incomplete micro-mixing but includes also the error of the analytical
558 method (Vanarase et al., 2013a). This short term variability was calculated by correcting the NIR
559 predictions for drifts using the curve fitting toolbox in MATLAB (Mathworks, Natick, Massachusetts, USA).
560 Despite, the impeller speed and configuration had no statistically significant impact on both the long and
561 short term variability. This is due to the narrow ranges that were observed for these mixing indices, 0.70-
562 1.10% and 0.65-0.80% respectively, which indicated excellent blend uniformity during steady state

563 processing. The limited difference between long and short term variability illustrated the continuous mixer
564 had sufficient axial mixing to filter out feeder fluctuations. Additionally, the root mean squared error of
565 prediction of the in-line NIR model was 0.24% which indicated that for a target drug load of 30% the lowest
566 achievable RSD would be around $0.24\%/30\% \approx 0.80\%$. Hence, one can conclude the best possible mixing
567 performance was achieved that could be detected with the employed analytical method.

568 **5.3.4 Tablet content uniformity**

569 Content uniformity ranged from 0.51 to 1.28% and indicated excellent micro-mixing performance. The
570 impeller configuration had a statistically significant effect on tablet content uniformity (figure 9, top).
571 However, this effect was nonlinear as reflected by the significant quadratic term. When the number of
572 RMB changed from 8 to 12, tablet content variability decreased marginally. However, equipping the
573 impeller with 16 RMB increased tablet content variability (e.g. 0.45% difference for 200 rpm respectively).
574 The impeller speed had no statistically and significant influence on content uniformity when it was varied
575 from its low to high setting. However, also for speed the quadratic term was significant indicating a curved
576 effect (figure 9, top). The interaction plot (figure 9, bottom) confirms that optimal homogeneity could be
577 achieved at intermediate impeller speed for a fixed impeller configuration. This can be attributed to the
578 maximum number of blade passes which the powder experienced at intermediate speed (figure 9, bottom).
579 However, the good correlation between content uniformity and strain for a fixed impeller configuration
580 (e.g. $R^2 = 0.91$ for 8 RMB) deteriorated when data obtained from multiple impeller configurations is
581 included ($R^2 = 0.45$). These findings suggest that not only the number of blade passes but also the number
582 of RMB on the impeller impacts micro-mixing and hence content uniformity.

583 **5.3.5 Tablet weight variability**

584 Tablet weight variability spanned a wide range from 2.07 to 4.77% within this design which underpinned
585 the impact of the blending process on tablet quality. The moderate to high tablet weight variation is due
586 to the poorly flowing Methocel CR-based formulation. The impact of improved blend properties, using
587 Methocel DC2, on tablet weight variability is described in section 5.5.2.1. However, for the more cohesive
588 Methocel CR-based formulation, the impeller configuration had a statistically significant influence on tablet
589 weight variability (figure 9, top). Tablets varied more in weight when the impeller was equipped with more
590 RMB. This impact of the impeller configuration was nonlinear and even intensified at high number of RMB.
591 This counterintuitive observation indicated that a higher fill level, prolonged mixing time and more blade
592 passes not necessarily resulted in improved blend properties for high speed tableting. Demixing of cohesive
593 blends was previously described for batch blending processes and was attributed to re-agglomeration or
594 compaction of the blend when the mixing time extended (Augsburger and Hoag, 2008). The higher levels

595 of strain associated with prolonged mixing may have compacted the blend and hence deteriorated the die
596 filling consistency and resulting in a higher tablet weight variation. Also mixing speed impacted weight
597 variation in a rather complex way (figure 9, top). For an impeller equipped with 16 RMB, mixing speed had
598 only a limited impact as weight variability was mostly dominated by the impeller design. For an intermediate
599 shear zone (12 RMB), the highest weight variability was observed when the impeller was set at intermediate
600 speed. This observation confirms that higher levels of strain can induce tablet weight variation. But
601 interestingly an interaction occurred when a high impeller speed was combined with low number of RMB
602 (figure 9, bottom) which resulted in high tablet weight variability. This observation suggests that still a
603 minimal fill level, mixing time and strain is required to achieve blend properties suitable for tableting. It is
604 clear that mixing time and strain need to be well balanced with tablet properties for the Methocel CR
605 formulation.

606 **5.3.6 Macro-mixing performance**

607 **5.3.6.1 Model based analysis**

608 A representative image of the variability on the active content in the feed stream was derived from an
609 extended run including multiple hopper refills (figure 10, left). Hence, the practical relevance of differences
610 in RTDs (section 5.3.1) can be evaluated by quantifying their ability to dampen both steady state flow rate
611 deviations and perturbations introduced by hopper refill. The variability in the feed stream remained
612 relatively low (1.07%). The relatively high screw speed (average ≈ 290 rpm) eliminated pulsation and
613 provided a fast response to perturbations, resulting in good precision (low variability) and high accuracy
614 (mean label claim 100.15%). All investigated blender settings were able to sufficiently dampen the observed
615 fluctuations in the inlet stream. The label claim range (i.e. difference between maximum and minimum) in
616 the outlet stream varied from 3.46% for the lowest axial mixing condition (8 RMB at 400 rpm) towards
617 1.44 % for the highest axial mixing condition (16 RMB at 200 rpm) which is significantly lower than the
618 label claim range in the feed stream (12.7 %). The model based analysis revealed the active content
619 variability in the outlet stream ranged from 0.32 to 0.59 %. The effect plot (figure 10, right) shows that
620 processing with more RMB or at lower speed clearly reduced label claim variability in the blender outlet
621 stream. The loading (figure 6) and effect plots confirmed this is due to a combination of more efficient axial
622 mixing (figure 8: higher péclet number and less tanks in series) and a higher residence time (figure 7: higher
623 bulk and mean residence time). In conclusion, the continuous blender has the proper design and process
624 ranges to filter out the noise introduced by the feeders and hence excellent macro-mixing performance
625 was achieved.

626 **5.3.6.2 Experimental analysis**

627 The macro-mixing performance was experimentally verified by content uniformity analysis of grab samples
628 collected at an interval of 10 s over an extended processing time (figure 11). Two runs were selected
629 based on their extreme axial mixing performance: 8 RMB at 400 rpm as low axial mixing or “lean”
630 condition, and 16 RMB at 200 rpm as high axial mixing or “robust” condition. The content uniformity was
631 0.49 and 0.61% for the high and low axial mixing setting, respectively. The average and individual tablet
632 content remained well within standard requirements. These findings supported our previous conclusions
633 regarding the excellent macro-mixing performance of the system. In conclusion, uniform tablet
634 characteristics were achieved during the steady state of the manufacturing process.

635 **5.4 Effect of drug load**

636 The NIR standards depicted in table 3 were processed using fixed settings. Changing drug load from 21.35
637 to 39.65% reduced fill level from 0.536 to 0.234 kg and hence also bulk residence time from 74 to 34 s.
638 Bulk density was the key material property impacting the fill level (figure 12, left) which indicates the
639 material was transported as a dense stirred powder bed under these conditions (16 RMB, 200 rpm). The
640 bulk density has been shown to be less influential when the powder bed is fluidized (e.g. at high impeller
641 speed) (Vanarase et al., 2013b). Blend uniformity ranged from 0.65 to 1.70 % suggesting good mixing
642 performance. Despite theoretically improved product (higher density and better flow) and process (higher
643 fill level and strain) responses, a lower content resulted in less homogenous blends (figure 12, right). It is
644 hypothesized this slightly reduced mixing performance can be attributed due to more challenging micro-
645 mixing inherently associated with the lower drug load. Furthermore, a higher level of strain has been shown
646 to adversely impact the distribution of the drug in the final HPMC CR product (section 5.3.3).

647 **5.5 Effect of HPMC grade and flow rate**

648 **5.5.1 Characterization of powder flow behavior in the continuous mixer**

649 **5.5.1.1 Effect of HPMC grade**

650 The RTD was estimated for both Methocel DC2 and CR-based formulations at various processing
651 conditions. The mixing time was slightly higher (+ 20 s) for the Methocel DC2-based formulation when
652 low mixing speed is combined with high number of RMB. Here the higher bulk density of the Methocel
653 DC2 formulation extended residence time within the mixer. This corresponds well with the previously
654 described (section 5.4) density-fill level relation and confirms the powder bed is in a dense regime under
655 these conditions. Furthermore, powder flow was in this regime best described by 2 tanks for both
656 formulations indicating the ratio of mixing and transport remained unaffected (figure 13, a). However when
657 the impeller was equipped with less RMB and/or operated at higher speed, considerably more tanks were

658 required to fit RTDs of the Methocel CR formulation compared to DC2 (figure 13, a). This indicated that
659 convective transport dominated over dispersive transport for the more cohesive Methocel CR formulation
660 under such conditions. The interaction between material properties and process parameters govern the
661 particle-particle dissipation rate and hence the powder flow behavior within the mixer. Overall, the axial
662 mixing efficiency was more robust to process changes for Methocel DC2 compared to CR.

663 **5.5.1.2 Effect of flow rate**

664 Processing the Methocel DC2-based formulation at higher flow rates increased the steady state fill level of
665 the blender (figure 14, left). The bulk residence time (figure 14, middle) and strain (figure 14, right)
666 decreased from 131 to 45 s and 412 to 170 revolutions when flow rate increased from 25 to 75 kg/h,
667 respectively. Although the difference in responses leveled off slightly between 50 and 75 kg/h, the mixer
668 did not yet reach its maximum fill level. The mixer could fill up more when the flow rate is set beyond the
669 investigated limit. However, the tablet press had a maximum capacity of 91 kg/h for this formulation, hence
670 the practical operational boundaries were covered within this study.

671 **5.5.2 Tablet quality**

672 **5.5.2.1 Tablet weight variability**

673 Figure 13b shows tablet weight variability is overall significantly lower when Methocel DC2 is used a matrix
674 former (1.44 – 1.79%) compared to CR (2.07– 4.77%). This can be attributed to the better flow of the
675 DC2 grade which yielded improved blend properties even at high drug load (section 5.1). The latter
676 resulted eventually in more consistent die filling and lower weight variability. Moreover, the Methocel DC2
677 formulation was more robust to changes in process and design variables. Figure 13b clearly shows that the
678 mixer speed and configuration had only a marginal impact on tablet weight variability using the DC2 grade.
679 This is an advantage compared to the Methocel CR formulation where low tablet weight variability (section
680 5.3.5) was only achieved at specific settings where other responses (e.g. axial mixing) were less optimal. It
681 is hypothesized that the better flowing Methocel DC2 formulation is not prone to demixing or compaction
682 phenomena during blending at high fill levels and hence die filling was more consistent. Furthermore, weight
683 variability remained comparable whilst operating at a flow rate of 25 (1.61%), 50 (1.50%) and 75 (1.72%)
684 kg/h. Despite the high drug load, the Methocel DC2 formulation flowed sufficiently for high speed tableting.
685 These findings illustrated that selecting appropriate excipient characteristics can enable continuous direct
686 compression of poorly flowing, low density APIs formulated at high drug load.

687 **5.5.2.2 Tablet content uniformity**

688 Although tablets with excellent uniformity could be manufactured using both formulations, the active
689 content for the Methocel DC2 formulation was more uniform and significantly more robust (figure 13c).

690 Furthermore, content uniformity for the DC2 grade remained excellent when the flow rate was increased
691 to 50 (0.74%) and 75 (0.71%) kg/h. Apparently, the micro-mixing performance was not significantly
692 impacted by flow rate despite the reduced strain and residence time (section 5.5.1.2).

693 **5.5.2.3 Tableability, compressibility, compactibility and axial recovery**

694 Tableability describes tensile strength as a function of applied compaction pressure (Patel et al., 2006).
695 Tablets were stronger when compressed at higher pressures (figure 15, a). The steep increase in strength
696 in the low pressure region is due to reduced tablet porosity upon particle rearrangements and volume
697 reduction, resulting in more bonding area. More immediate axial recovery was observed at higher
698 compaction pressures (figure 15, b) as the porosity was already reduced and a further increase of pressure
699 induced elastic deformation of particles. Elastic recovery occurred after compression thereby weakening
700 interparticulate bonding (Sun and Grant, 2001). Consequently, the tableability curve gradually leveled off.

701 Formulations with Methocel CR as matrix former showed superior compaction behavior compared to
702 Methocel DC2. It is hypothesized that the smaller particles of the CR grade resulted in a higher packing
703 density and more contact points between particles, thereby improving inter-particle bonding and yielding
704 a better tableability (Sun and Himmelsbach, 2006; Thoorens et al., 2014). Tablet strength is determined
705 by bonding area and bonding strength per unit bonding area. Contributions from each of these factors
706 cannot be separated by means of the tableability curves. Therefore the compressibility and compactibility
707 was evaluated in order to understand the observed differences in tableting behavior. Compressibility is the
708 ability of a material to undergo volume reduction as a result of an applied pressure, whereas compactibility
709 normalizes tablet strength by porosity. The Methocel CR-based formulation exhibited more
710 compressibility compared to the Methocel DC2 formulation processed at the same flow rate (figure 15,
711 c). At the same compaction pressures, tablet porosity was consistently lower which is correlated to a
712 higher bonding area within a tablet. For all profiles, the tensile strength was negatively correlated with
713 porosity (figure. 15, d). Although Methocel CR-based formulations exhibited a better tableability, its
714 compactibility curve partially overlapped the Methocel DC2 curve. This observation suggested that its
715 greater compressibility is at the origin of the better tableability of Methocel DC2. Therefore, the superior
716 tableability is a result of its greater bonding area and not of its greater bonding strength per unit bonding
717 area.

718 Another observation is the strain rate sensitivity of the Methocel DC2 formulation: a change in flow rate
719 from 25 to 75 kg/h yielded weaker tablets when the compaction pressure remained constant. In a
720 continuous process, increasing the flow rate affected each unit operation. Operating at higher flow rate
721 reduced RTD and strain in the continuous blenders and tablet press feed frame. As a result the lubricant

722 mixing time is reduced which potentially improved tableability. Also the dwell time during main
723 compression decreased from 15.90 to 5.30 ms at higher flow rate as the turret needed to rotate at higher
724 speed (27 to 82 rpm) to maintain the correct mass balance. As some deformation processes are time
725 dependent, a prolonged dwell time results in more plastic deformation, leading to more consolidation. In
726 this case, the net effect of the longer lubrication and prolonged dwell time improved tableability, indicating
727 that the reduced dwell time is the dominating factor for the observed strain rate sensitivity. Tablets
728 compacted with longer dwell time showed improved compressibility. As plastic deformation is time
729 dependent, the volume reduction and hence increase in bonding area is more important when dwell time
730 was longer. In addition, the overlapping compactibility profiles indicated that bonding strength per unit
731 bonding area was not significantly influenced by dwell time. Studying tableability, compressibility and
732 compactibility profiles highlighted the importance of porosity. One can manufacture tablets with similar
733 tensile strength by targeting equal tablet porosity.

734 **5.5.2.4 Drug release**

735 The impact of compaction pressure and flow rate on drug release from Methocel DC2-based formulation
736 was investigated by means of a two level full factorial screening design. Figure 16 shows drug release over
737 16 h and the fit of the applied model. To elucidate which tablet properties steer the dissolution rate, the
738 responses derived from the dissolution profiles (section 4.4.2.5) and their corresponding tablet properties
739 (section 4.4.2.2) were both included. A PLS model was fit: the loading plot (figure 5.17) revealed the
740 experimental responses clustered. This indicates the time to reach 20 and 50% drug release was highly
741 correlated ($R^2=0.99$). Interestingly, the release exponent of the dissolution model co-varied with these
742 experimental responses ($R^2= 0.95-0.98$). By contrast, the kinetic constant of the dissolution model lies on
743 the opposite side of the straight line that connects the origin with the cluster of dissolution responses.
744 This indicates the kinetic constant is negatively correlated with the release exponent ($R^2 = -0.99$) and the
745 time to reach 20 ($R^2 = -0.99$) and 50% ($R^2 = -0.97$) drug release. The high correlation between experimental
746 and model based dissolution responses indicated that the power law model was adequate to describe drug
747 release. Moreover, the experimental and simulated dissolution data correlated well ($R^2 > 0.99$) and
748 confirmed the suitability of the model. The release exponent ranged between 0.46 and 0.51, indicating
749 diffusion-controlled drug release.

750 The experimental design revealed that compaction pressure significantly affected dissolution responses and
751 tablet properties. Levina and Rajabi-Siahboomi (2004) described that the sensitivity of drug release to
752 compaction pressure depended upon the compressibility of the formulation: in matrices with lower
753 porosity the water uptake and water front movement was slower, which reduced the drug release rate.
754 Also in the current study, drug release was significantly slower at higher compaction pressure which was

755 reflected by lower values for the kinetic constant but higher values for release exponent and a prolonged
756 time to reach 20 and 50% time drug release. Compacting at higher pressure reduced tablet thickness, area
757 and porosity, whereas tablet strength and hardness improved. These observations combined resulted in a
758 slower drug release. Based on their correlation with dissolution responses, the importance of tablet
759 properties could be ranked from high to low as: tablet area, thickness, tensile strength, hardness and
760 porosity. Tablet area was previously reported to steer the release rate (Li et al., 2005) and hence thickness
761 was a simple tablet property that correlated well with all dissolution responses (R^2 : 0.90 to 0.95). Ensuring
762 low thickness variation during manufacturing of sustained release tablets is hence crucial.

763 The rate of drug release was relatively slow as the cumulative release was limited to about 60% after 16h.
764 One of the research goals was to elucidate the impact of HPMC grade on tablet properties. To this extent,
765 a high percentage of HPMC was selected in the model formulation to evoke potential differences in blend
766 and tablet properties. This relatively low drug-to-polymer ratio extended the drug release (Li et al., 2005).
767 Altering the ratio of tablet surface area and weight was a simple tool to accelerate drug release: 80% drug
768 was released after 16 h when this ratio increased with only 14%. Future work can focus on steering the
769 rate of drug release from continuously produced matrix tablets by modifying the ratio and physico-chemical
770 properties of HPMC and fillers (Levina and Rajabi-Siahboomi, 2004).

771 **6 Conclusions**

772 This study presented a framework for process and product development on a continuous direct
773 compression platform. The ability to continuously manufacture sustained release tablets was explored
774 using a formulation with high drug load of a poorly flowing low density API. Each unit operation was
775 thoroughly investigated to reveal how design aspects, process settings and material properties impacted
776 the process behavior and product quality. Two HPMC matrices were evaluated: standard Methocel CR
777 and direct compressible DC2. Characterization revealed the DC2 grade flowed better than CR and yielded
778 eventually improved blend properties. The capacity of feeding correlated directly with the density of the
779 materials. Determining the feed factor and flow rate requirement allowed to estimate drive command
780 which rationalized the selection of screw pitch. Most materials showed a limited feed factor decay and
781 were emptied till 20% fill level before triggering a refill. By contrast, more compressible powders initiated
782 the decay at higher fill levels and were as a consequence refilled at 40% fill level. Inline NIRs was shown to
783 be an adequate tool for RTD estimation and process monitoring. The blender possessed good macro-
784 mixing capabilities as NIRs suggested excellent blend uniformity during steady state processing. The model-
785 based analysis of macro-mixing performance confirmed the RTD was able to dampen the observed feeder
786 fluctuations. In addition, the excellent mixing performance was confirmed experimentally by analyzing the

787 content of tablets sampled over an extended sampling time. The experimental design with Methocel CR
788 revealed the impeller configuration had a significant impact on the powder flow within the mixer. Extending
789 the shear zone restricted powder transport and enhanced dispersion which resulted in a higher residence
790 time and fill level, yielding thereby more strain and optimal axial mixing efficiency. The effect of speed on
791 mixing and transport of powder was more pronounced at high filling degree. Higher conveying rates shifted
792 RTD curves to the left, while fill level, strain and axial mixing efficiency were reduced. Furthermore, bulk
793 density was a key blend property during as a higher density resulted in a higher fill level during blending.

794 Using Methocel CR, the axial mixing and strain needed to be well balanced with tablet properties. Tablet
795 quality deteriorated when more axial mixing was achieved through extending the shear zone on the
796 impeller. However an impeller with small shear zone achieved optimal tablets with low weight and content
797 variability when the applied strain was maximized via the impeller speed. A higher robustness to changes
798 in the blending process was achieved with Methocel DC2. The better flow of the Methocel DC2 blend
799 yielded overall lower tablet weight and content variability and enabled manufacturing at 75 kg/h. This
800 observation underpinned the importance of flow during continuous blending and die-filling. Blends with
801 Methocel CR showed better tableability driven by a higher compressibility that originates from its higher
802 bonding area. However, tablets of similar strength could be produced with Methocel DC2 by targeting
803 equal porosity. Controlling thickness during continuous manufacturing of sustained release tablets
804 appeared to be crucial.

805 **7 References**

- 806 Armstrong, N.A., Haines-Nutt, R.F., 1972. Elastic recovery and surface area changes in compacted powder
807 systems. *J. Pharm. Pharmacol.* 24, 135–136.
- 808 Augsburger, L.L., Hoag, S.W., 2008. *Pharmaceutical dosage forms - Tablets*, Third. ed.
- 809 Cartwright, J.J., Robertson, J., D’Haene, D., Burke, M.D., Hennenkamp, J.R., 2013. Twin screw wet
810 granulation: Loss in weight feeding of a poorly flowing active pharmaceutical ingredient. *Powder*
811 *Technol.* 238, 116–121. doi:10.1016/j.powtec.2012.04.034
- 812 Engisch, W., Muzzio, F., 2015. Using Residence Time Distributions (RTDs) to Address the Traceability of
813 Raw Materials in Continuous Pharmaceutical Manufacturing. *J. Pharm. Innov.* 11, 64–81.
814 doi:10.1007/s12247-015-9238-1
- 815 Engisch, W.E., Muzzio, F.J., 2015. Feedrate deviations caused by hopper refill of loss-in-weight feeders.
816 *Powder Technol.* 283, 389–400. doi:10.1016/j.powtec.2015.06.001
- 817 Engisch, W.E., Muzzio, F.J., 2014. Loss-in-Weight Feeding Trials Case Study: Pharmaceutical Formulation.
818 *J. Pharm. Innov.* 10, 56–75. doi:10.1007/s12247-014-9206-1
- 819 Engisch, W.E., Muzzio, F.J., 2012. Method for characterization of loss-in-weight feeder equipment. *Powder*
820 *Technol.* 228, 395–403. doi:10.1016/j.powtec.2012.05.058
- 821 Ervasti, T., Simonaho, S.-P., Ketolainen, J., Forsberg, P., Fransson, M., Wikström, H., Folestad, S., Lakio, S.,
822 Tajarobi, P., Abrahamsén-Alami, S., 2015. Continuous manufacturing of extended release tablets via
823 powder mixing and direct compression. *Int. J. Pharm.* 495, 290–301.
824 doi:10.1016/j.ijpharm.2015.08.077
- 825 Fogler, S., 2006. *Elements Of Chemical Reaction Engineering.*, Fourth. ed. Pearson international.
- 826 Fonteyne, M., Vercruyse, J., De Leersnyder, F., Van Snick, B., Vervaet, C., Remon, J.P., De Beer, T., 2015.
827 Process Analytical Technology for continuous manufacturing of solid-dosage forms. *TrAC Trends*
828 *Anal. Chem.* 67, 159–166. doi:10.1016/j.trac.2015.01.011
- 829 Gao, Y., Vanarase, A., Muzzio, F., Ierapetritou, M., 2011. Characterizing continuous powder mixing using
830 residence time distribution. *Chem. Eng. Sci.* 66, 417–425. doi:10.1016/j.ces.2010.10.045
- 831 Järvinen, K., Hoehe, W., Järvinen, M., Poutiainen, S., Juuti, M., Borchert, S., 2013. In-line monitoring of the
832 drug content of powder mixtures and tablets by near-infrared spectroscopy during the continuous

- 833 direct compression tableting process. *Eur. J. Pharm. Sci.* 48, 680–8. doi:10.1016/j.ejps.2012.12.032
- 834 Järvinen, M.A., Paaso, J., Paavola, M., Leiviskä, K., Juuti, M., Muzzio, F., Järvinen, K., 2013. Continuous direct
835 tablet compression: effects of impeller rotation rate, total feed rate and drug content on the tablet
836 properties and drug release. *Drug Dev. Ind. Pharm.* 39, 1802–8. doi:10.3109/03639045.2012.738681
- 837 Kuentz, M., Leuenberger, H., 1999. Pressure susceptibility of polymer tablets as a critical property: a
838 modified Heckel equation. *J. Pharm. Sci.* 88, 174–9. doi:10.1021/js980369a
- 839 Kumar, A., Vercruyssen, J., Toiviainen, M., Panouillot, P.-E., Juuti, M., Vanhoorne, V., Vervaet, C., Remon,
840 J.P., Gernaey, K. V., De Beer, T., Nopens, I., 2014. Mixing and transport during pharmaceutical twin-
841 screw wet granulation: experimental analysis via chemical imaging. *Eur. J. Pharm. Biopharm. Off. J.*
842 *Arbeitsgemeinschaft für Pharm. Verfahrenstechnik e.V* 87, 279–89. doi:10.1016/j.ejpb.2014.04.004
- 843 Kumar, A., Vercruyssen, J., Vanhoorne, V., Toiviainen, M., Panouillot, P.-E., Juuti, M., Vervaet, C., Remon,
844 J.P., Gernaey, K. V., De Beer, T., Nopens, I., 2015. Conceptual framework for model-based analysis
845 of residence time distribution in twin-screw granulation. *Eur. J. Pharm. Sci.* 71, 25–34.
846 doi:10.1016/j.ejps.2015.02.004
- 847 Levenspiel, O., 1999. *Chemical reaction engineering*, Third. ed.
- 848 Levina, M., Rajabi-Siahboomi, A.R., 2004. The influence of excipients on drug release from hydroxypropyl
849 methylcellulose matrices. *J. Pharm. Sci.* 93, 2746–54. doi:10.1002/jps.20181
- 850 Li, C.L., Martini, L.G., Ford, J.L., Roberts, M., 2005. The use of hypromellose in oral drug delivery. *J. Pharm.*
851 *Pharmacol.* 57, 533–46. doi:10.1211/0022357055957
- 852 Meier, R., Thommes, M., Rasenack, N., Moll, K.-P., Krumme, M., Kleinebudde, P., 2016. Granule size
853 distributions after twin-screw granulation - do not forget the feeding systems. *Eur. J. Pharm.*
854 *Biopharm.* doi:10.1016/j.ejpb.2016.05.011
- 855 Patel, S., Kaushal, A.M., Bansal, A.K., 2006. Compression physics in the formulation development of tablets.
856 *Crit. Rev. Ther. Drug Carrier Syst.* 23, 1–65.
- 857 Peeters, E., 2015. Investigation of the tableting process in continuous production: influence of feeding and
858 extended dwell time during compression on dependent process variables and tablet properties.
859 Ghent University.
- 860 Pernenkil, L., Cooney, C.L., 2006. A review on the continuous blending of powders. *Chem. Eng. Sci.* 61,

- 861 720–742. doi:10.1016/j.ces.2005.06.016
- 862 Portillo, P.M., Ierapetritou, M.G., Muzzio, F.J., 2008. Characterization of continuous convective powder
863 mixing processes. *Powder Technol.* 182, 368–378. doi:10.1016/j.powtec.2007.06.024
- 864 Siepmann, J., Peppas, N.A., 2012. Modeling of drug release from delivery systems based on hydroxypropyl
865 methylcellulose (HPMC). *Adv. Drug Deliv. Rev.* 64, 163–174. doi:10.1016/j.addr.2012.09.028
- 866 Simonaho, S.-P., Ketolainen, J., Ervasti, T., Toiviainen, M., Korhonen, O., 2016. Continuous manufacturing
867 of tablets with PROMIS-line - Introduction and case studies from continuous feeding, blending and
868 tableting. *Eur. J. Pharm. Sci.* doi:10.1016/j.ejps.2016.02.006
- 869 Sun, C., Grant, D.J.W., n.d. Influence of Crystal Structure on the Tableting Properties of Sulfamerazine
870 Polymorphs. *Pharm. Res.* 18, 274–280. doi:10.1023/A:1011038526805
- 871 Sun, C.C., Himmelpach, M.W., 2006. Reduced tableting of roller compacted granules as a result of
872 granule size enlargement. *J. Pharm. Sci.* 95, 200–6. doi:10.1002/jps.20531
- 873 Thoorens, G., Krier, F., Leclercq, B., Carlin, B., Evrard, B., 2014. Microcrystalline cellulose, a direct
874 compression binder in a quality by design environment--a review. *Int. J. Pharm.* 473, 64–72.
875 doi:10.1016/j.ijpharm.2014.06.055
- 876 Vanarase, A.U., Alcalà, M., Jerez Rozo, J.I., Muzzio, F.J., Romañach, R.J., 2010. Real-time monitoring of drug
877 concentration in a continuous powder mixing process using NIR spectroscopy. *Chem. Eng. Sci.* 65,
878 5728–5733. doi:10.1016/j.ces.2010.01.036
- 879 Vanarase, A.U., Järvinen, M., Paaso, J., Muzzio, F.J., 2013a. Development of a methodology to estimate
880 error in the on-line measurements of blend uniformity in a continuous powder mixing process.
881 *Powder Technol.* 241, 263–271. doi:10.1016/j.powtec.2013.02.012
- 882 Vanarase, A.U., Muzzio, F.J., 2011. Effect of operating conditions and design parameters in a continuous
883 powder mixer. *Powder Technol.* 208, 26–36. doi:10.1016/j.powtec.2010.11.038
- 884 Vanarase, A.U., Osorio, J.G., Muzzio, F.J., 2013b. Effects of powder flow properties and shear environment
885 on the performance of continuous mixing of pharmaceutical powders. *Powder Technol.* 246, 63–72.
886 doi:10.1016/j.powtec.2013.05.002
- 887 Vercruyse, J., Delaet, U., Van Assche, I., Cappuyns, P., Arata, F., Caporicci, G., De Beer, T., Remon, J.P.,
888 Vervaet, C., 2013. Stability and repeatability of a continuous twin screw granulation and drying system.

889 Eur. J. Pharm. Biopharm. Off. J. Arbeitsgemeinschaft für Pharm. Verfahrenstechnik e.V 85, 1031–8.
890 doi:10.1016/j.ejpb.2013.05.002

891 Yu, L.X., Amidon, G., Khan, M.A., Hoag, S.W., Polli, J., Raju, G.K., Woodcock, J., 2014. Understanding
892 pharmaceutical quality by design. AAPS J. 16, 771–83. doi:10.1208/s12248-014-9598-3

893

894 **Acknowledgements**

895 The authors are grateful to Ms. Liesa Pollet of Ghent University and Mr. Tim Derr and Mr. Scott Vass of
896 Colorcon Inc. for their many hours of analytical work in support of this project. Ivan Bogaerts, Marc
897 Lattem, Alexander Schaepman and Tomas Vermeire (GEA APC pharma solids) are acknowledged for
898 providing access and technical support on the GEA CDC-50.

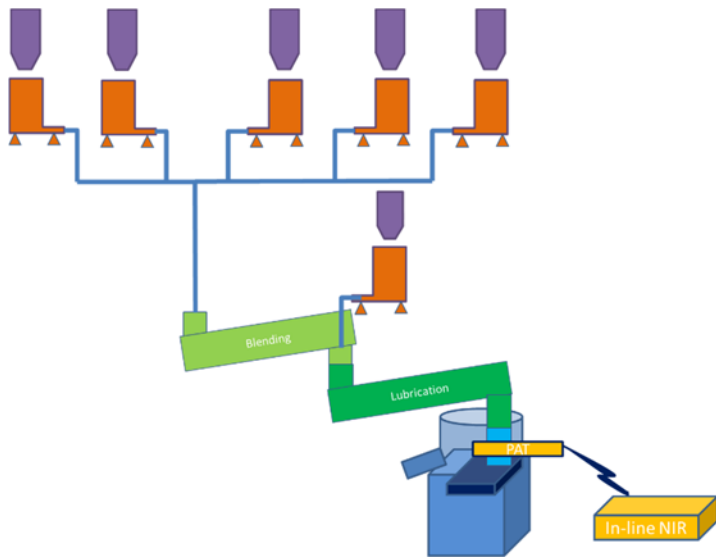


Figure 1: Flowsheet of CDC-50. Powder supply and refill mechanism (■), twin screw feeding (■), blending (■), lubrication (■), feed tube (■), in-line NIRs as PAT tool (■) and tablet press (■).

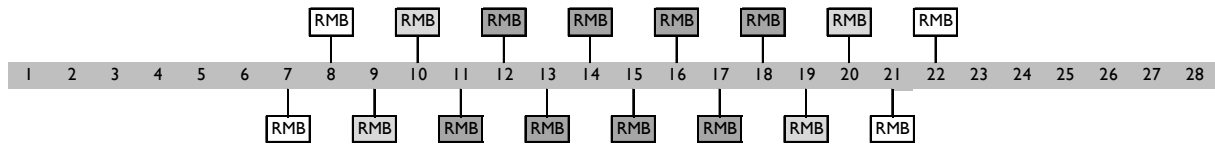


Figure 2: Schematic presentation of an impeller equipped with 8 RMB (RMB) and extensions to 12 (RMB) and 16 (RMB) RMB. The RMB were centered on the impeller whereas remaining blades were positioned in full transport orientation.

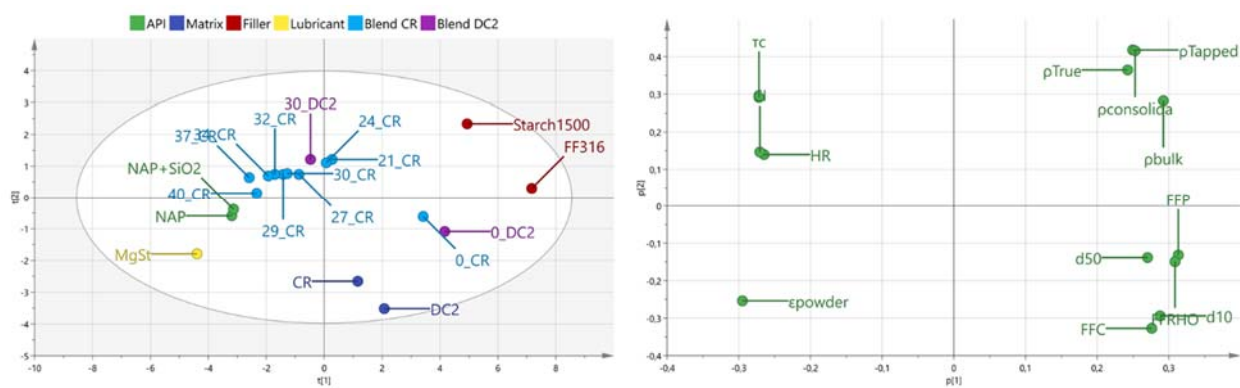


Figure 3: Scores (left) and loadings plot (right) of PCA model describing material properties. Observations on score plot are colored according to their functionality and blends are labeled according to NAP+SiO₂ content and HPMC grade. The abbreviations of properties on the loading plot are described in methods section.

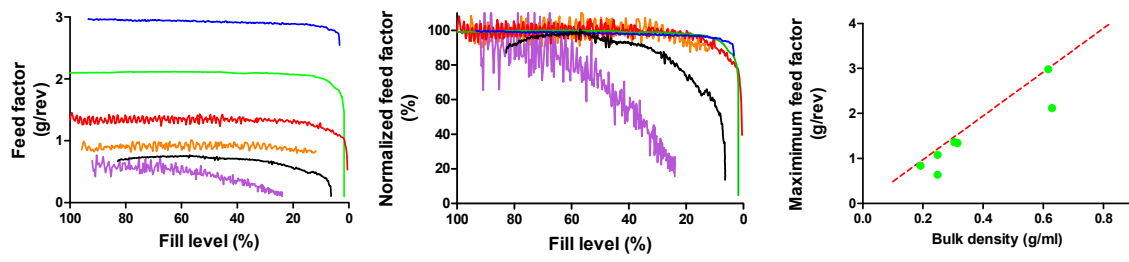


Figure 4: Feed factor (left) and normalized feed factor (middle) decay as a function of hopper fill level (%) using concave screws with 20 mm pitch. Starch I 500 (—), FF316 (—), Methocel DC2(—), NAP+SiO₂(—), MgSt (—) and NAP (—). Right: theoretical (- - -) and experimental (●) density-feed factor relation.

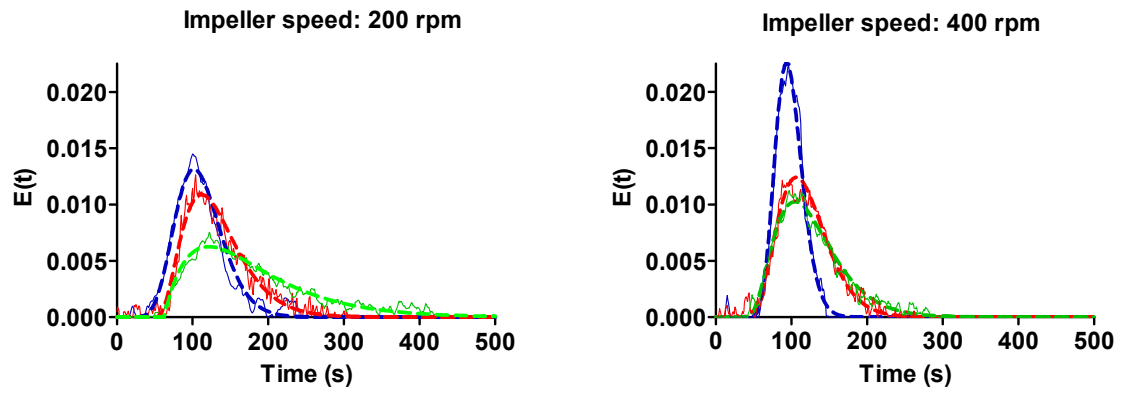


Figure. 5: Experimental RTD (—) and model fit (---) using tanks in series with plug-flow volume fraction model. Impeller equipped with 8 (---), 12 (---) and 16 (---) RMB operating at 200 (left) and 400 (right) rpm.

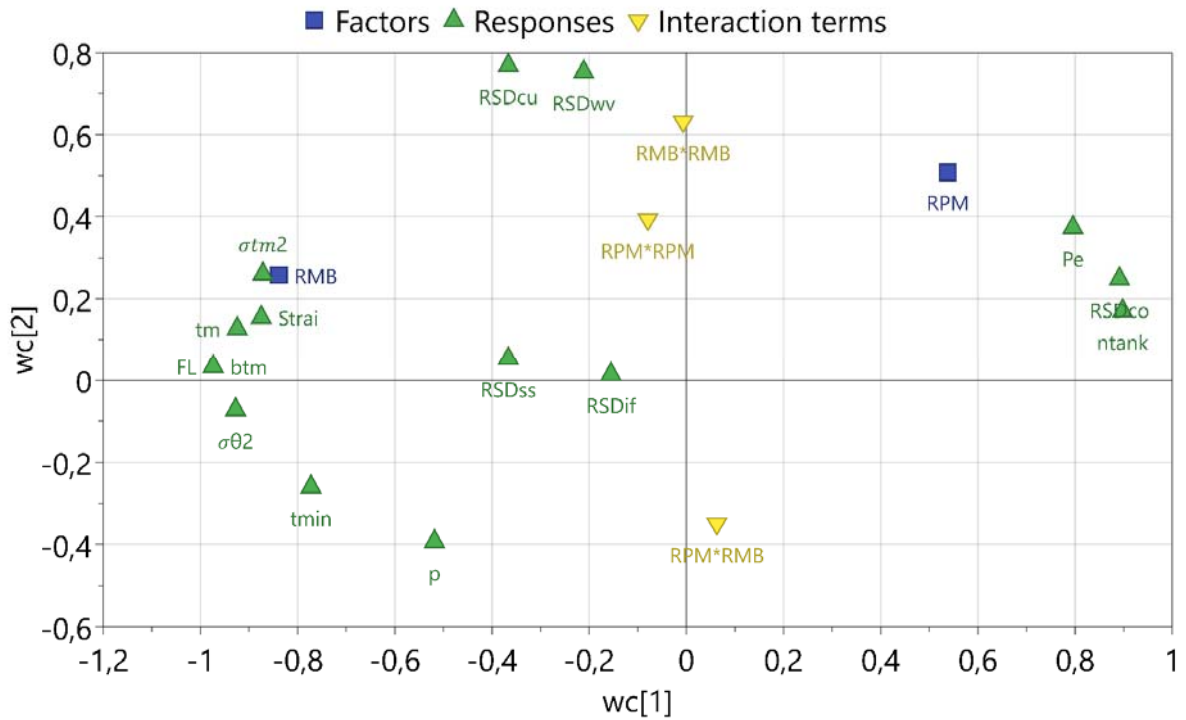


Figure 6: Blending DOE: loading plot of PLS model. RMB and RPM denote impeller configuration and impeller speed. The responses corresponding to the abbreviations are described below and ranked according to their R^2 : Fill level = 1.00 (FL), bulk residence time = 1.00 (btm), strain or number of blade passes = 1.00 (Strai), number of tanks in series = 0.96 (n_{tanks}), model based macro-mixing performance or $RSD_{\text{Cout}} = 0.93$ (RSD_{co}), Péclet = 0.92 (Pe), mean residence time = 0.92 (tm), variance = 0.91 (σ_{tm^2}), normalized variance = 0.90 (σ_{θ^2}), tablet content uniformity = 0.88 (RSD_{cu}), tablet weight variation = 0.84 (RSD_{wv}), minimum residence time = 0.78 (tmin), plug-flow volume fraction = 0.56 (p), short term blend uniformity = 0.54 (RSD_{if}), steady state blend uniformity = 0.38 (RSD_{ss}).

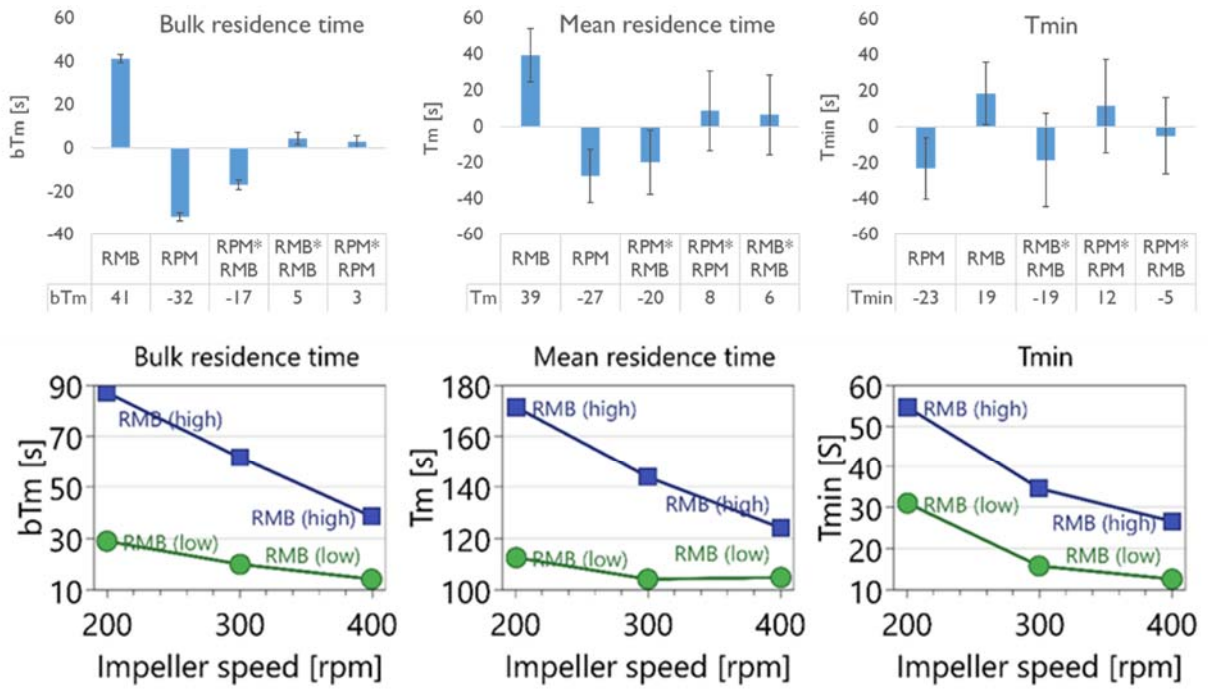


Figure 7: Blending DOE: effect (above) and interaction (below) plot for responses bulk residence time (left), mean (t_m , middle) and minimum time (t_{min} , right). The table presents the size of the effect.

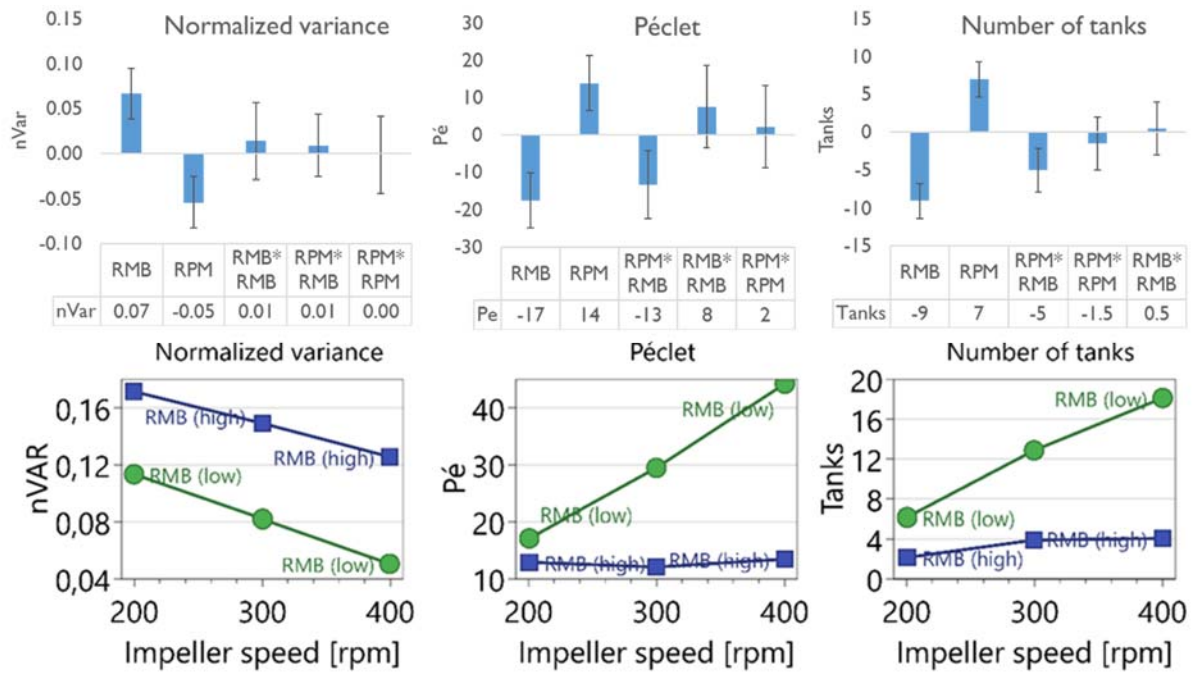


Figure 8: Blending DOE: effect (above) and interaction (below) plot for responses normalized variance (σ_{θ}^2 , left), péclet (Pe , middle) and number of tanks (n_{tanks} , right). The table presents the size of the effect.

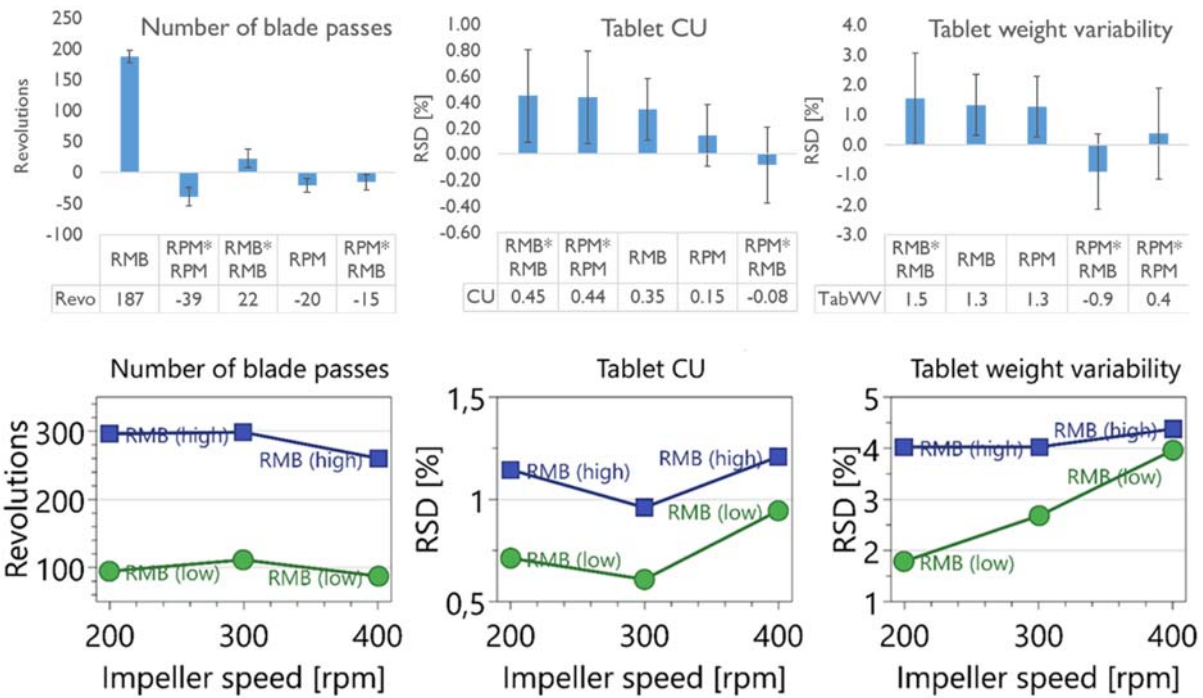


Fig 9: Blending DOE: effect (above) and interaction (below) plot for responses strain (left), tablet CU (RSD_{cu} , middle) and tablet weight variability (RSD_{wv} , right). The table presents the size of the effect.

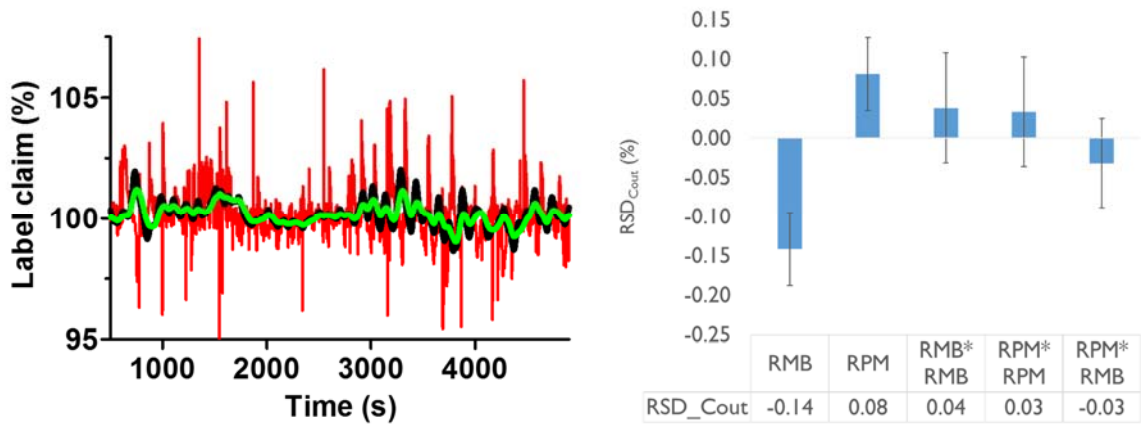


Figure 10: RTD model based macro-mixing evaluation. Left: NAP+SiO₂ (%) label claim as a function of time in feed stream (—) and in blender outlet stream using 8 (—) and 16 RMB (—) at 400 rpm. Right: Blending DOE: effect size and plot for response NAP+SiO₂ (%) variability in outlet stream (RSD_{Cout}).

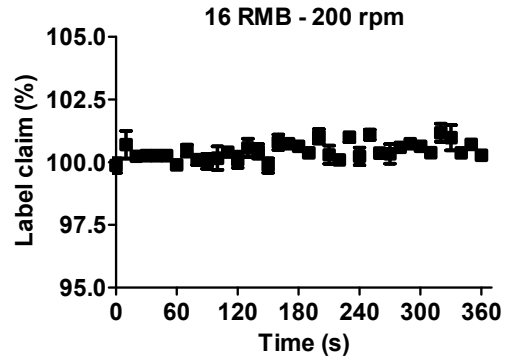
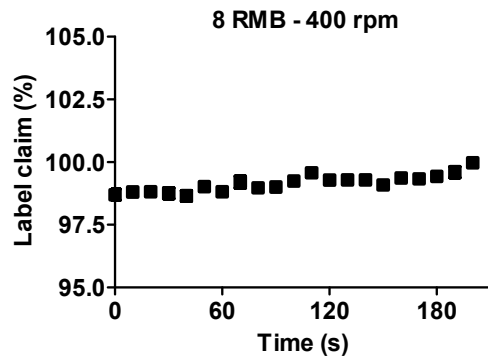


Figure 11: Content uniformity analysis as macro-mixing verification. Mean tablet content (n=10) and RSD (error bars) as function of process time. Left and right represent low and high axial mixing condition.

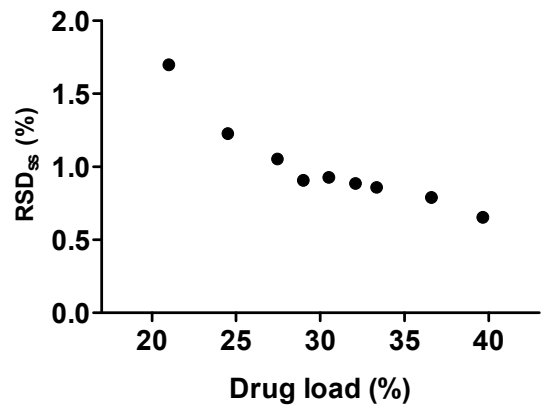
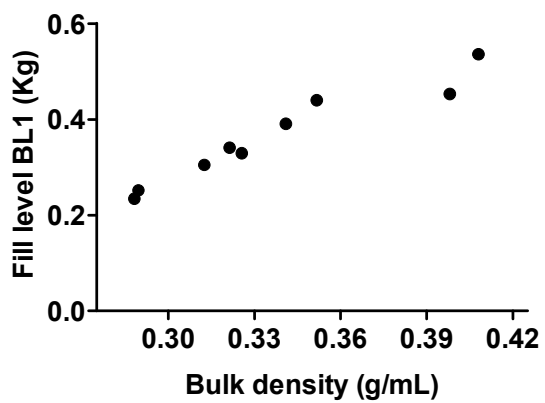


Figure 12: Left: impact of the bulk density of the blend on the steady state fill level in the continuous mixer. Right: steady state blend uniformity determined via NIRs as a function of drug load.

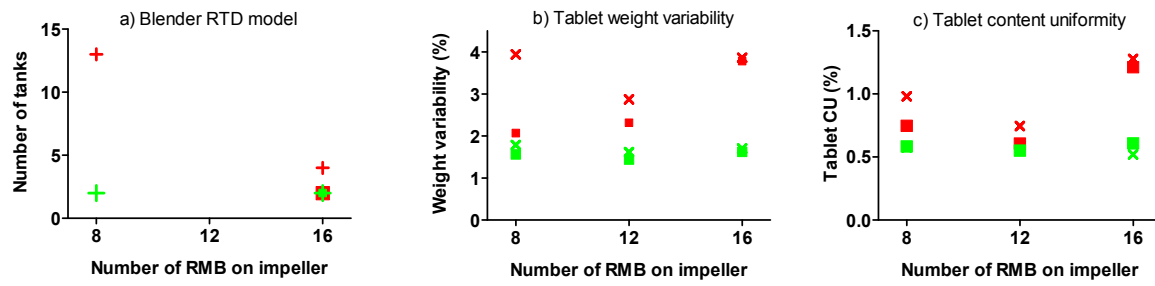


Figure 13: Impact of HPMC grade on process and product responses: a) Number of tanks for optimal model fit of blender RTD, b) tablet weight variability, c) tablet content uniformity. Legend: (x) DC2 – 400 rpm, (+) DC2 – 300 rpm, (■) DC2 – 200 rpm, (x) CR – 400 rpm, (+) CR – 300 rpm and (■) CR – 200 rpm.

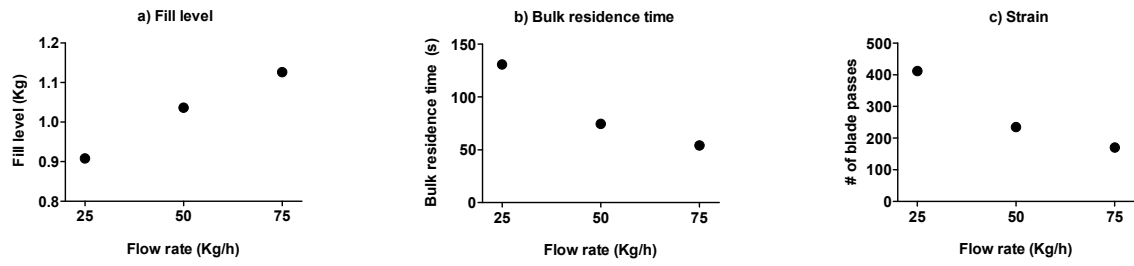


Figure 14: Effect of flow rate on fill level (a), bulk residence time (b) and number of blade passes (c) in blender I (●).

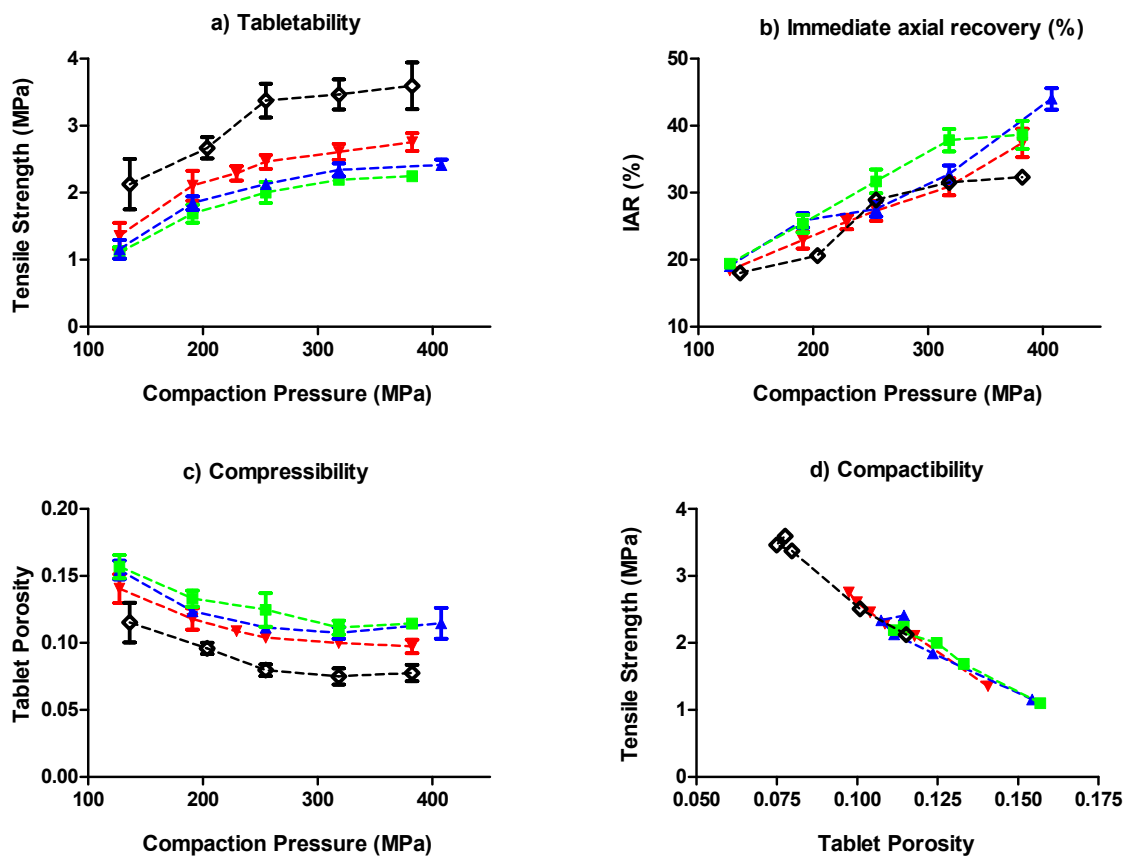


Figure 15: Tableability (a), immediate axial recovery (b), compressibility (c) and compactibility (d) plot for HPMC DC2 processed at 25 (\blacktriangledown), 50 (\blacktriangle) and 75 (\blacksquare) kg/h and HPMC CR (\diamond) at 25 kg/h. Error bars indicate standard deviation (n=10).

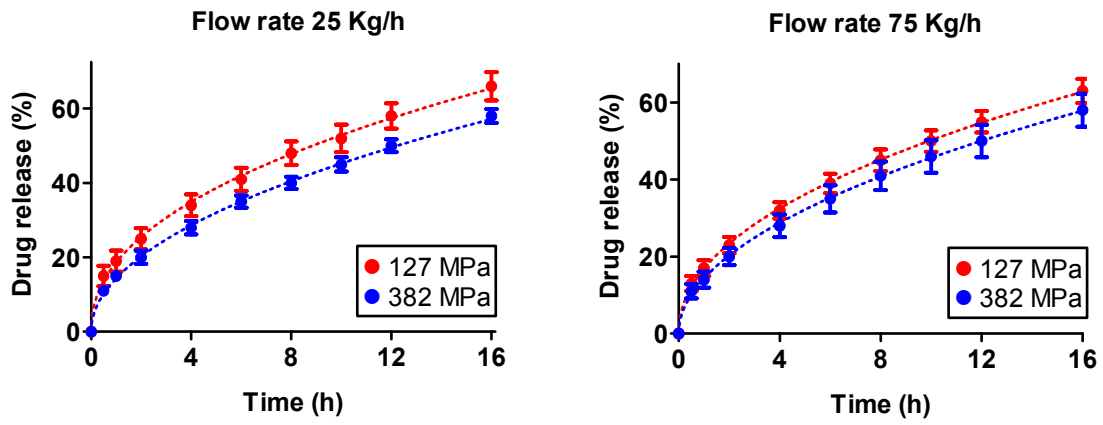


Figure 16: Experimental drug release (●) and model fit (---). Flowrate set at 25 (left) and 75 (right) kg/h. Color coding according to main compaction pressure.

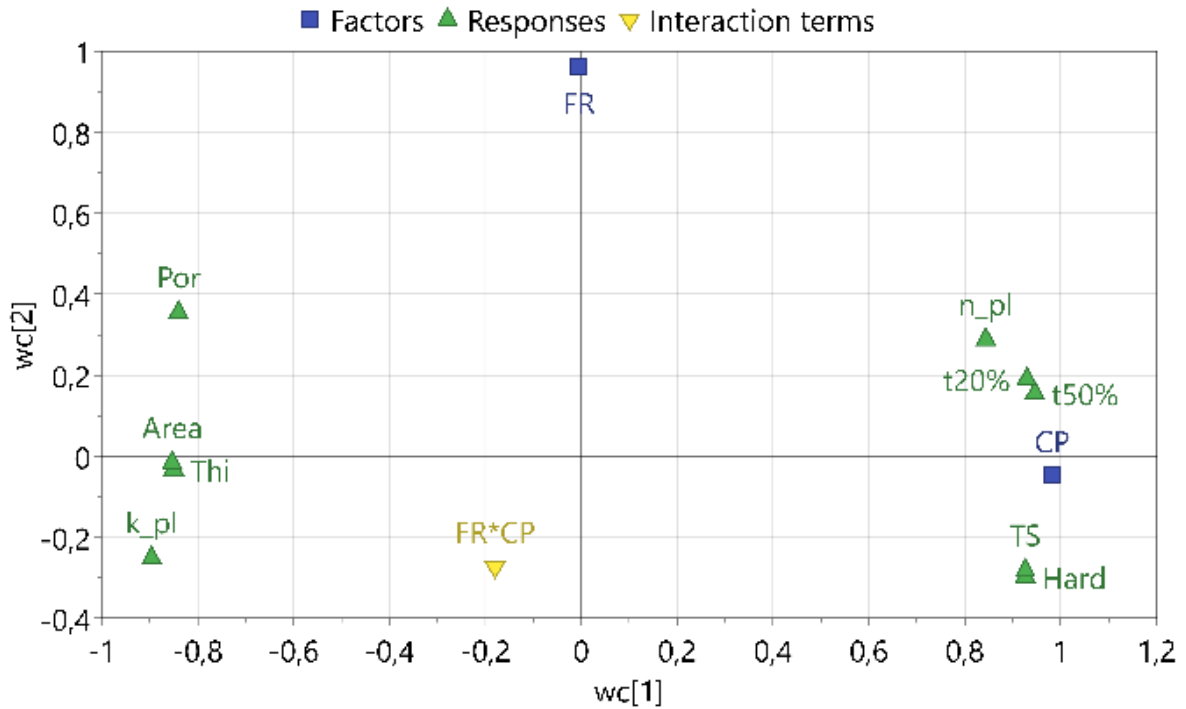


Figure 17: Tablet quality DOE: loading plot of PLS model. Responses and abbreviations ranked according to R^2 : tensile strength (TS) = 0.94, hardness (Hard) = 0.94, time to release 50% drug (t50%) = 0.92, time to release 20% drug (t20%) = 0.90, kinetic constant power law model (k_pl) = 0.87, tablet porosity (Por) = 0.83, release exponent power law model (n_pl) = 0.79, tablet area (Area) = 0.73, thickness (Thi) = 0.72. The factors compaction pressure and flow rate were abbreviated as CP and FR.

Material	ff_p	ρ_{bulk}	ffc	d50	HR
Methocel CR	1.46	0.30	4.81	82	1.36
Methocel DC2	1.95	0.31	6.18	102	1.27
FF316	4.81	0.63	7.64	88	1.13
NAP	0.36	0.25	1.43	13	1.37
NAP+SiO ₂	0.57	0.25	2.28	13	1.76
MgSt	0.42	0.19	2.21	8	1.65
Starch I500	2.35	0.62	3.81	65	1.29

Table 1. Key material properties of individual raw materials.

Material	Flow rate range (kg/h)	Screw pitch (mm)	Max feed factor (g/revolution)	Drive command (%) at flow rate ranges
Methocel CR	7.5 – 22.5	20	1.36	20.0 – 59.9
Methocel DC2	7.5 – 22.5	20	1.34	20.1 – 60.4
FF316	7.25 – 21.75	20	2.12	12.3 – 37.0
MgSt	0.125 – 0.375	20	0.84	0.5 – 1.6
MgSt	0.125 – 0.375	10	0.35	1.3 – 3.9
NAP	7.5 – 22.5	20	0.64	42.2 – 126.5
NAP+SiO2	7.75 – 22.88	20	1.08	25.9 – 76.4
Starch I500	2.5 – 7.5	20	2.98	3.0 – 9.1
Starch I500	2.5 – 7.5	10	1.48	6.1 – 18.3

Table 2. Overview of flow rate ranges covered in this study and their corresponding drive command estimated using the maximum feed factor. A screw speed of 462 rpm corresponds to 100% drive command.

Target (%w/w)	Predicted (%w/w)	Bias (%w/w)	RMSEP(%w/w)
21.00	20.84	0.16	0.40
24.50	24.41	0.09	0.31
27.45	27.34	0.11	0.29
28.98	28.79	0.19	0.33
30.5 - "Day 1"	30.49	0.01	0.44
30.5 - "Day 2"	30.49	0.01	0.26
30.5 - "Day 3"	30.35	0.15	0.34
32.08	31.12	0.96	1.00
33.35	34.37	-1.02	0.86
36.60	37.30	-0.70	0.76
39.65	39.26	0.39	0.46

Table 3. Verification of in-line NIRs blend uniformity model: NAP target and predicted concentration, bias and RMSEP.

